



HAL
open science

Crustal complexity in the Lachlan Orogen revealed from teleseismic receiver functions

Fabrice R. R. Fontaine, Hrvoje Tkalčić, Brian L. N. Kennett

► To cite this version:

Fabrice R. R. Fontaine, Hrvoje Tkalčić, Brian L. N. Kennett. Crustal complexity in the Lachlan Orogen revealed from teleseismic receiver functions. *Australian Journal of Earth Sciences*, 2013, 60 (3), pp.413-430. 10.1080/08120099.2013.787646 . hal-01308542

HAL Id: hal-01308542

<https://hal.univ-reunion.fr/hal-01308542v1>

Submitted on 28 Apr 2016

HAL is a multi-disciplinary open access archive for the deposit and dissemination of scientific research documents, whether they are published or not. The documents may come from teaching and research institutions in France or abroad, or from public or private research centers.

L'archive ouverte pluridisciplinaire **HAL**, est destinée au dépôt et à la diffusion de documents scientifiques de niveau recherche, publiés ou non, émanant des établissements d'enseignement et de recherche français ou étrangers, des laboratoires publics ou privés.

1 **CRUSTAL COMPLEXITY IN THE LACHLAN OROGEN**
2 **REVEALED FROM TELESEISMIC RECEIVER**
3 **FUNCTIONS**

4 Fabrice R. Fontaine^{a,+}, Hrvoje Tkalčić^b, and Brian L.N. Kennett^b

5 ^a Laboratoire GéoSciences Réunion, Université de La Réunion, Institut de Physique du
6 Globe de Paris, Sorbonne Paris Cité, UMR 7154 CNRS, Univ Paris Diderot, F-97715
7 Saint Denis, France. fabrice.fontaine@univ-reunion.fr

8 ^b Research School of Earth Sciences, Australian National University, Canberra, ACT
9 0200, Australia. hrvoje.tkalcic@anu.edu.au; brian.kennett@anu.edu.au

10

⁺ **Corresponding author:**

E-mail: fabrice.fontaine@univ-reunion.fr

10 Abstract

11 There is an ongoing debate about the tectonic evolution of southeast Australia,
12 particularly about the causes and nature of its accretion to a much older Precambrian
13 core to the west. Seismic imaging of the crust can provide useful clues to address this
14 issue. Seismic tomography imaging is a powerful tool often employed to map elastic
15 properties of the Earth's lithosphere, but in most cases does not constrain well the depth
16 of discontinuities such as the Mohorovičić (Moho). In this study, an alternative imaging
17 technique known as receiver function (RF) has been employed for seismic stations near
18 Canberra in the Lachlan Orogen to investigate: (i) the shear wave velocity profile in the
19 crust and uppermost mantle, (ii) variations in the Moho depth beneath the Lachlan
20 Orogen, and (iii) the nature of the transition between the crust and mantle. A number of
21 styles of RF analyses were conducted: H-K stacking to obtain the best compressional-
22 shear velocity (V_P/V_S) ratio and crustal thickness; non-linear inversion for the shear
23 wave velocity structure and inversion of the observed variations in RFs with back-
24 azimuth to investigate potential dipping of the crustal layers and anisotropy.

25 The thick crust (up to 48 km) and the mostly intermediate nature of the crust-mantle
26 transition in the Lachlan Orogen could be due to the presence of underplating at the
27 base of the crust, and possibly to the existing thick piles of Ordovician mafic rocks
28 present in the mid and lower crust. Results from numerical modelling of receiver
29 functions at 3 seismic stations (CAN, CNB and YNG) suggest that the observed
30 variations with back-azimuth could be related to a complex structure beneath these
31 stations with the likelihood of both a dipping Moho and crustal anisotropy. Our analysis
32 reveals crustal thickening to the west beneath CAN station which could be due to slab
33 convergence. The crustal thickening may also be related to the broad Macquarie

34 volcanic arc, which is rooted to the Moho. The crustal anisotropy may arise from a
35 strong N-S structural trend in the eastern Lachlan Orogen and to the preferred
36 crystallographic orientation of seismically anisotropic minerals in the lower and middle
37 crust related to the palaeo-Pacific plate convergence.

38 **Key words:** crustal thickness; Moho; seismic anisotropy; Lachlan Orogen, receiver
39 function, seismic structure, crustal complexity

40

41 **1. Introduction**

42 The Middle Palaeozoic Lachlan Orogen (450-340 Ma) in southeastern Australia
43 (Figures 1a, 1b & 1c) was accreted to the Precambrian core of the continent in a
44 sequence of stages, (e.g. Collins 2002a; Direen & Crawford 2003; Gray & Foster 2004).
45 There is ongoing debate as to the exact causes and the nature of accretion. The main
46 reasons are the complexity of the crustal structure of the Lachlan Orogen, and the
47 limited constraints on the crustal structure (particularly on the lower crust). Indeed, only
48 a few deep seismic refraction and reflection profiles have been conducted in the region
49 (e.g. Finlayson et al. 1980; Direen et al. 2001; Finlayson et al. 2002; Glen et al. 2002).
50 Most onshore refraction profiles date from the 1960s to 1980s (see e.g. Kennett et al.
51 2011). The crustal structure is constrained in few locations from passive seismic
52 experiment: receiver functions studies (Shibutani et al. 1996; Clitheroe et al. 2000;
53 Kennett et al. 2011). An anisotropic upper, middle and lower crust was well imaged in
54 previous seismic reflection data (Direen et al. 2001; Glen et al. 2002) and the seismic
55 interface between the crust and the mantle was interpreted as not flat (Finlayson et al.
56 2002; Glen et al. 2002).

57 In this paper, we bring new constraints on the complex crustal structure in the
58 Lachlan Orogen and particularly in the Canberra region, where we have three
59 permanent stations quite close to each other: CAN at Mt Stromlo, CNB in Kowen
60 Forest and YNG at Young. We also exploit the portable station SO01 to the west near
61 Lake Cargelligo. We show evidence for both crustal anisotropy and a dipping Moho in
62 an area south of the earlier seismic reflection studies.

63

64 **2. Data analysis (CAN, CNB, YNG and SO01 stations)**

65 The receiver function technique depends on the analysis of the conversions between
66 seismic wave types and reverberations following the onset of major seismic phases,
67 commonly the first arriving P wave from distant earthquakes. The sequence of
68 secondary arrivals carries information about the structure beneath the recording station.
69 The effects of the source, and the major part of the propagation path, can be eliminated
70 by deconvolving the vertical component of motion by the radial component directed
71 along the great-circle to the source (Langston 1977, 1979). The resulting *radial receiver*
72 *function* is then dominated by P to S conversions and crustal multiples which are
73 diagnostic of the nature of crustal structure.

74 Many of the methods of RF analysis are based on the assumption that the structure
75 beneath the seismic station can be adequately represented by horizontal stratification,
76 with either uniform layers or gradient zones separated by discontinuities in seismic
77 wavespeed at which conversions arise between P and S waves. We have used three
78 different styles of analysis that exploit various features of the RF waveform, and
79 emphasise different crustal features: crustal thickness, presence of intra-crustal seismic
80 discontinuities, nature of the Moho, V_P/V_S ratio, dipping structure and anisotropy.

81 A) H-K STACKING METHOD FOR MOHO DEPTH AND AVERAGE CRUSTAL
82 PROPERTIES

83 The seismic reverberations in the crust and the delays between P and S waves can
84 constrain crustal thickness and the compressional wave/shear wave velocity ratio
85 (V_P/V_S). At stations where both the Pms (the P to S conversion at the Moho) and the
86 $PpPms$ (the first Moho multiple) phases are observed, we use a robust grid-search stack
87 procedure (Zhu & Kanamori 2000) to determine the mean Moho depth and mean crustal
88 V_P/V_S ratio (for details see the supplementary materials). This approach depends on
89 good knowledge of the mean crustal velocity. For southeastern Australia we have good
90 constraints from seismic refraction work (Drummond & Collins 1986) and employ an
91 average crustal velocity $V_P = 6.65$ km/s (for station CAN see Figure 2, for station CNB
92 see Figure 3, and for station SO01 see Figure 4). We use stacks of all receiver functions
93 across all back-azimuths, and select only events with signal-to-noise ratio (SNR) ≥ 5 in
94 order to increase the visibility of multiple phases.

95 B) NONLINEAR WAVEFORM INVERSION FOR RF

96 The radial receiver functions at each seismic station were stacked for a set of back-
97 azimuths, with a narrow range of ray-parameters based on the following procedure (see
98 Fontaine et al. 2013 for further details):

99 (1) Select the quadrant (back-azimuths between $N0^\circ$ - $N90^\circ$, $N90^\circ$ - $N180^\circ$, $N180^\circ$ -
100 $N270^\circ$, $N270^\circ$ - $N360^\circ$) with the highest number of RFs.

101 (2) Compute p_{median} : the median of the ray parameters of all seismic events in this
102 interval.

103 (3) Select events with a ray parameter = $p_{\text{median}} \pm 0.004$ (s/km). Most data come
104 from seismogenic belts surrounding Australia and this narrows down the range of useful

105 ray parameters. For example, the useful ray parameter range for station CAN is between
106 0.067 and 0.075 s/km.

107 (4) Stack the RFs selected in the previous step. Only mutually coherent RFs are used
108 for stacking and we focused on obtaining the most basic information assuming a
109 horizontally layered structure. Before each stack we checked the coherency of
110 individual RFs using the cross-correlation matrix approach from Tkalčić et al. (2011)
111 and we found insignificant difference of crustal thickness derived from the NA
112 inversion of a single RF and the inversion of the stacked RF at the same station.

113 We have used a nonlinear inversion method, the Neighbourhood Algorithm (NA,
114 Sambridge 1999), to determine the crust and upper mantle structure that can explain the
115 observed radial RF with a 1-D seismic velocity model. During the inversion, the
116 synthetic radial RF for the layered structure was calculated using the Thomson-Haskell
117 matrix method (Thomson 1950; Haskell 1953). The full effects of free-surface
118 reverberations and conversions were modelled. During the inversion, as in the work of
119 Shibutani et al. (1996) the model was parameterised in terms of 6 layers: a sediment
120 layer, basement layer, upper crust, middle crust, lower crust, and uppermost mantle with
121 internal velocity gradients and the possibility of discontinuities at the boundaries. We
122 used similar bounds for the 24 parameters to those of Shibutani et al. (1996), Clitheroe
123 et al. (2000) and Fontaine et al. (2013) (e.g. Table 1 of Fontaine et al. 2013). The
124 inversion is carried out in terms of 24 parameters, the V_S values at the top and bottom of
125 the gradient zone, the thickness of the gradient zone and the V_P/V_S ratio in each zone.
126 The inclusion of the V_P/V_S ratio serves primarily to allow for some of the effects of the
127 sedimentary layer beneath the stations with no a priori information (Bannister et al.
128 2003). The NA method combines a Monte Carlo search technique and the properties of

129 the Voronoi geometry in parameter space to find an ensemble of the best fitting models
130 and performs a global optimization. We present the results of inversions through density
131 plots of the best 1000 data fitting S -velocity models generated by the neighbourhood
132 algorithm (see, e.g. Figures 5, 6). The model with the best fit to the data is plotted in
133 red. The set of 24 parameters in the inversion are relatively well-constrained, but the S -
134 velocity distribution is better constrained by the inversion than the V_P/V_S ratio.

135 C) ANALYSIS FOR ANISOTROPY AND DIPPING LAYERS

136 For isotropic and horizontally layered structures, the theoretical transverse receiver
137 functions are zero. For either an isotropic dipping layer or an anisotropic layer, the
138 transverse RFs do not vanish. The polarity of the direct P phase and the Pms phase on
139 the transverse component can constrain the direction of discontinuity dip (Peng and
140 Humphreys 1997). A periodicity of 360° with respect to back-azimuth in Pms amplitude
141 can be caused by a dipping interface or by an anisotropic layer with a tilted axis of
142 symmetry. In contrast, a 180° periodicity in Pms amplitude is produced by crustal
143 anisotropy with transverse anisotropy and a horizontal symmetry axis.

144 At station CAN, radial and transverse receiver functions show evidence (Figure 7)
145 for both the presence of crustal anisotropy and a dipping Moho. We employ the
146 neighbourhood algorithm as implemented by Frederiksen et al. (2003) for the joint
147 inversion of the radial and transverse receiver functions for models with both anisotropy
148 and dipping structure. We assumed the presence of both a dipping Moho and an
149 anisotropic lower, middle and upper crust with hexagonal symmetry. Hexagonal
150 symmetry is specified by a symmetry axis orientation and 5 independent elastic
151 constants for a total of seven free parameters. Hexagonal symmetry can occur in Earth

152 from several different mechanisms (e.g. Sherrington et al. 2004). Effective hexagonal
153 anisotropy may be due to:

- 154 (1) thin alternating layers of fast and slow material when the seismic wavelength
155 is substantially greater than the layer,
- 156 (2) aligned cracks within an isotropic rock, and
- 157 (3) preferred mineral alignments if there is a single preferred orientation, with
158 random orientations in the other two coordinates, even when the individual
159 minerals have higher order symmetry.

160 Although cracks may be important at shallow depths, several studies have found that
161 aligned minerals are the most likely cause of seismic anisotropy in rocks at middle and
162 lower crustal depths (e.g. Siegesmund et al. 1989; Kern & Wenk 1990; Barruol & Kern
163 1996; Weiss et al. 1999). Most natural lower continental rocks show hexagonal type of
164 anisotropy (Weiss et al. 1999).

165 The synthetic seismograms used in the inversion are computed using a ray-based
166 approach (Frederiksen & Bostock 2000). Multiples were not computed primarily to
167 minimize computation time, which could take several hours if all multiples are included
168 (e.g. Sherrington et al. 2004). The inversion starts by randomly choosing some number
169 of models from a multidimensional model parameter space. The user defines the size of
170 the model parameter space by defining the range of each model parameter. Synthetic
171 seismograms are computed for each model and cross correlation based misfits between
172 data and the synthetics are calculated. As the number of iteration increases the smaller
173 regions of model parameter space containing low misfit are searched in more detail. We
174 consider two anisotropic layers in the crust and one isotropic sedimentary layer on the
175 top with less than 2 km thickness to simplify the computation. We allowed the level of

176 velocity anisotropy to vary between 0 and 10%. Savage (1998) proposed that anisotropy
177 should be small in the upper crust based on results from local earthquake shear-wave
178 splitting studies with less than 4% anisotropy in the top few kilometres of the crust
179 (Crampin 1994). Layer thicknesses and velocity ranges were fixed using constraints
180 from Finlayson et al. (2002) and Glen et al. (2002).

181 **3. Results**

182 A) H-K STACKING RESULTS FOR MOHO DEPTH AND V_p/V_s

183 We were able to use the H-K stacking method to constrain crustal thickness and the
184 V_p/V_s ratio at four stations (SO01, CNB, YNG and CAN), at the others (in the Lachlan
185 Orogen) we could not observe clear multiples. Chevrot & van der Hilst (2000) have
186 previously pointed out the absence of clear multiples in this region. At CAN station, we
187 obtain the best stack for an apparent crustal thickness of 26 km (Figure 2b); however the
188 associated V_p/V_s value of 1.58 is almost implausible as a significant portion of the crust
189 would have to be composed of quartz (Christensen 1996). Interestingly, we observe a
190 local maximum for a depth of 39 km with $V_p/V_s=1.72$, which is much closer to the
191 results at CNB and YNG seismic stations. These values are physically more realistic
192 and more consistent with the results from the other modelling methods that we used in
193 this study; and also similar to those by Chevrot & van der Hilst (2000) who obtained a
194 Moho depth of 37 km and a V_p/V_s ratio value of 1.72 at CAN. The reason that the H-K
195 stacking concentrates on a shallower seismic discontinuity than the Moho, determined
196 by the other RF methods, is due to the assumption of a single layered crust and a sharp
197 base of the crust at a station where the crust-mantle transition is gradational. The crustal
198 thickness estimates from H-K stacking are: 39 ± 2 km at station CNB (Figure 3b), 35 ± 6
199 km at station YNG (see supplementary Figure 1) and 39 ± 2 km at station SO01 (Figure

200 4b). We obtain V_p/V_s ratios of 1.72 ± 0.08 , 1.70 ± 0.03 , 1.75 ± 0.11 and 1.78 ± 0.04 for
201 stations CAN, CNB, YNG and SO01.

202 B) NON-LINEAR INVERSION RESULTS

203 To constrain the Moho depth, we have used the neighbourhood algorithm
204 (Sambridge 1999) considering 5 layers with gradients in the crust at all stations. We
205 take the base of the transition to mantle velocities to define the Moho depth, in order to
206 be in accordance with previous RF studies (e.g. Clitheroe et al. 2000) which produce
207 Moho depths close to estimates from seismic refraction studies (Collins 1991; Collins
208 et al. 2003). Here, we take the upper mantle velocity for this Phanerozoic region to be
209 $V_p \geq 7.6$ km/s following Giese (2005), which means that $V_s \geq 4.3 - 4.4$ km/s for V_p/V_s
210 ratios in the range 1.73-1.77 at the base of the gradient. In previous Australian studies
211 Clitheroe et al. (2000) used similar values ($V_p > 7.6$ km/s) for receiver functions, and
212 Collins et al (2003) used for their compilation, with both refraction and receiver
213 function results, a value of $V_p > 7.8$ km/s. Fontaine et al. (2013) confirmed that using
214 $V_p \geq 7.6$ km/s (i.e $V_s \geq 4.3-4.4$ km/s assuming a V_p/V_s ratio in the range 1.73-1.77) and
215 the base of the zone of velocity gradients provides good agreement between crustal
216 thicknesses estimated from seismic reflection profiles and those obtained from receiver
217 function inversion.

218 Figures 5 and 6 present the shear wave velocity models from the NA inversion and
219 data fits at SO01, CAN, CNB and YNG. Figure 8 compares the average shear wave
220 velocity models beneath CAN, CNB and YNG. We obtained similar depths to the
221 Moho using different methods: the base of a gradient at 48 km from the NA algorithm
222 (Figure 5 and supplementary Figure 2) and 43-49 km from an alternative grid search
223 (see supplementary materials) with a single sharp discontinuity.

224 The Moho depths show a generally thick crust beneath this part of the Lachlan
225 Orogen ranging from 34 km in the west and up to 48 km (Figure 9). Taking into account
226 crustal thickness estimates from previous studies (e.g. Clitheroe et al. 2000; Collins et
227 al. 2003; Kennett et al. 2011; Fontaine et al. 2013), the maximum crustal thickness is
228 thicker beneath the Lachlan Orogen than beneath the Gawler Craton. Fontaine et al.
229 (2013) found a maximum crustal thickness of 45 km beneath the Gawler Craton
230 whereas we found a value of 48 km beneath CAN and YNG stations in the Lachlan
231 Orogen. The uncertainty of a crustal thickness value is mainly between 2 and 3 km
232 (Fontaine et al. 2013). The lower crustal structures obtained at CAN and YNG
233 correspond to a broad velocity transition zone at the Moho and a crustal thickness
234 around 48 km. The results of Moho depths (45 and 47 km) from NA inversion at CNB
235 and SO01 are compatible with results obtained from the grid search stacking (Moho
236 depths of 39 ± 2 km and 39 ± 2 km).

237

238 C) DETAILED MODELLING OF RFS AND THEIR VARIATIONS AT 239 PERMANENT STATIONS (CAN, CNB AND YNG)

240 The receiver functions at CAN and YNG display a 360° periodicity of the direct *P*
241 phase in back-azimuth (Figures 7 and 10), which suggests a dipping Moho structure or
242 a tilted anisotropic layer. In the case of an isotropic medium with a dipping crustal
243 discontinuity, the dip direction is the direction for which the amplitude of the direct *P*-
244 wave on the transverse component goes from negative to positive values (Peng &
245 Humphreys 1997). At CAN, the dip direction would be 270° ; this would imply a strike
246 of 180° for the discontinuity.

247 The relative behaviour of the radial and transverse RFs at CAN suggests the

248 presence of anisotropy: we observe a clear difference in arrival time between the radial
249 and transverse *Pms* phase at CAN (Figure 7) which is a strong indication of splitting of
250 the shear wave converted at the Moho. The observed delay time is 0.21 s for the *Pms*
251 phase for RFs with a back-azimuth of 65°.

252 At CAN we have good coverage of back-azimuth, and the patterns of variation in
253 amplitude on the transverse RFs, relative to the direct *P* phase suggest the presence of
254 both dipping structure and crustal anisotropy (Figure 7). The back-azimuthal coverage
255 is not as good at CNB, but the transverse RFs (Figure 11) are not negligible and suggest
256 the presence of either an isotropic dipping discontinuity and/or anisotropic crustal layer.
257 Interestingly, the RFs variations show a 360° periodicity of the *Pms* phase at station
258 YNG (Figure 10) suggesting the presence of a dipping Moho or crustal anisotropy with
259 a dipping axis of symmetry. The amplitude of the direct *P* phase is negative on the
260 transverse components for back-azimuths between -65° and 95°, whereas it is positive
261 on the radial components. This feature is not expected for a simple isotropic crust with a
262 dipping discontinuity and suggests the presence of crustal anisotropy with a dipping
263 symmetry axis (see Figure 5b in Savage 1998). The presence of a negative pulse on the
264 transverse component for the direct *P* phase might be due to the fact that both the upper
265 and the lower crust are anisotropic (see Figure 5b and 5c in Savage 1998). The
266 amplitude of the transverse component is quasi-null for back-azimuths near 85°. Such
267 RFs variations with back-azimuth could be related to crustal anisotropy with a slow axis
268 direction close to 85° and thus the fast axis direction near -5° (i.e 355°), which is
269 consistent with the fast axis direction obtained at station CAN. This E-W direction of
270 the slow axis is also consistent with the highest amplitude of the *Pms* phase on the
271 radial components for a back-azimuth of 95°. We note a change of polarity of the *Pms*

272 phase on the transverse component at -120° (i.e 240°) and at 60° . This change of
273 polarity with a 360° periodicity may be related to a Moho dipping in the WSW direction
274 (240°).

275 Although RF inversion is both non-linear and non-unique, the observed features
276 (polarity and delay) of the direct P phase and the Pms phase on radial and transverse
277 components are compatible with RFs synthetics that we computed for simple dipping
278 anisotropic structures with the inversion method of Frederiksen et al. (2003). The
279 average of the best 100 fitting-models from the 18000 models generated during the
280 inversion of receiver functions is given in Table 1. This average model is our preferred
281 model based on the global optimization used for the inversion. Table 2 gives the best-
282 fitting model from all models generated during the inversion of receiver functions. The
283 best-fitting model at station CAN is presented in Figure 12 as synthetic radial and
284 transverse RFs versus back-azimuth. We present in the Table 3 the range of values
285 associated with anisotropy and a dipping Moho determined for the best 100 models.
286 Both the strike and the dipping angle values obtained for the Moho (Table 1, 2 and 3)
287 are similar to the values obtained from seismic reflection profiles in the eastern Lachlan
288 Orogen (Glen et al. 2002) north of the Canberra region. The dipping angle is also
289 consistent with Moho depth determined in this study at CAN and CNB stations from the
290 neighbourhood algorithm inversion of radial receiver function. The Moho is dipping to
291 the east of CAN and the fast symmetry axis direction is between 0 and 13° in the upper
292 anisotropic layer and between 309 and 352° in the lower anisotropic layer. The axis of
293 symmetry dips in the range 0 to 7° in the upper anisotropic layer and between 16 and
294 24° in the lower anisotropic layer. Anisotropy with a dipping symmetry axis can
295 produce a pattern identical to that caused by a dipping interface in an isotropic medium.

296 It is difficult to distinguish between a dipping axis of symmetry and a dipping interface
297 for a single station from receiver functions alone (Savage 1998) or from particle motion
298 alone (Schulte-Pelkum et al. 2001).

299 **4. Discussion**

300 Our analysis of the RFs provides information on the nature of the crust through the
301 V_p/V_s ratio, on the nature of the Moho and constraints on dipping structures and
302 anisotropy.

303 A) V_p/V_s RATIOS

304 We observe significant variations in the V_p/V_s ratio across the region. At SO01 the
305 V_p/V_s value obtained from the H-K stacking is high (V_p/V_s is ca. 1.78) in the crust
306 suggesting a mafic composition compatible with mafic granulite rocks (Christensen
307 1996). The V_p/V_s ratio is around 1.7 at CAN and CNB and 1.75 at YNG compatible
308 with the presence of granite-gneiss beneath CAN and CNB and biotite gneiss beneath
309 YNG. This would be the down dip extension of mafic rocks imaged and modelled in
310 Figure 4a & 4b of Direen et al. (2001). At CAN and CNB stations, the V_p/V_s values are
311 compatible with mafic orthogneisses or mafic granulite inferred in the lower crust from
312 a wide-angle seismic profile in the southern Lachlan Orogen (Finlayson et al. 2002).
313 Whereas at YNG station the V_p/V_s value is compatible with paragneisses inferred from
314 seismic reflection profiles performed across the Junee-Narromine Volcanic Belt in the
315 vicinity of this seismic station (Direen et al. 2001).

316 B) NATURE OF THE CRUST-MANTLE TRANSITION

317 Using the character of the crust-mantle transition (Figures 5c, 5d, 6c and 6d) we
318 classify the Moho transition zone as sharp ≤ 2 km, intermediate 2-10 km, or broad ≥ 10
319 km, as suggested by Shibutani et al. (1996). Our Moho estimates lie at the base of any

320 gradient (in conformity with earlier work (e.g. Clitheroe et al. 2000). The crust-mantle
321 boundary is deep and mostly intermediate in character beneath the Lachlan Orogen.
322 These results are consistent with previous observations (e.g. Shibutani et al. 1996;
323 Clitheroe et al. 2000; Collins et al. 2003; Fontaine et al. 2013). Finlayson et al. (2002)
324 pointed out a sharper velocity gradient to the upper mantle velocity in the north than in
325 the south. The authors preferred interpretation was that there may be a velocity
326 transition zone, 1-3 km thick, at the base of the lower crust rather than a step increase in
327 velocity, with a thicker, more diffuse zone in the south and thus closer to CAN and
328 CNB stations (point A of Figure 1c). The broad velocity transition zone at the Moho
329 obtained for both CAN and CNB are thus in agreement with the interpretation of
330 Finlayson et al. (2002). The thickened crust beneath the Lachlan Orogen was already
331 established by previous studies (e.g. Shibutani et al. 1996; Clitheroe et al. 2000; Collins
332 et al. 2003; Fontaine et al. 2013). The variations in the crustal thickness and the
333 intermediate and broad transition between crust and mantle beneath the Lachlan Orogen
334 may be related to the presence of underplating at the base of the crust (e.g. Drummond
335 & Collins 1986; Shibutani et al. 1996; Gray & Foster 2004; Fontaine et al. 2013). They
336 may also result from existing thick piles of Ordovician mafic rocks present in the mid
337 and lower crust (Glen et al. 2002). As proposed in previous studies (O'Reilly 1989; Cull
338 et al. 1991; McDonough et al. 1991) based on heat-flow models and the predominant
339 mafic lower crustal rock types identified in xenoliths, magmatic and tectonic
340 underplating has been a significant mechanism in the crustal growth. Finlayson et al.
341 (2002) and Glen et al. (2002) also suggested from a seismic refraction profile the
342 presence of an underplated layer near CAN and CNB. Interestingly, the tomographic
343 model from Rawlinson et al. (2010) shows an increase of *P*-wavespeed at the SO01

344 location and the authors interpret the high velocity zone as a result of the presence of
345 magmatic underplating.

346 C) DIPPING MOHO

347 The behaviour of the receiver functions at CAN suggests a dipping Moho to the
348 west beneath CAN station, and this ties with a thinner Moho at CNB (Figure 8). A
349 dipping Moho was also imaged by previous seismic studies. Finlayson et al. (2002)
350 from a seismic refraction profile and Glen et al. (2002) from a seismic reflection profile
351 show a southerly dip of the Moho. Glen et al. (2002) also show from seismic reflection
352 profiles a west dipping Moho with a dipping angle between 2 and 3°, which is in
353 agreement with our results. The crustal thickening towards the west might be due to the
354 slab convergence (of the palaeo-Pacific plate). The thickening could also be due to the
355 broad semi-autochthonous Macquarie volcanic arc, which is rooted to the Moho. It would
356 be good to have further information from closer to the coast, but such seismic stations
357 suffer from much higher ambient seismic noise and so a long duration of recording is
358 necessary to extract high-quality receiver function information.

359 D) EVIDENCE FOR ANISOTROPIC STRUCTURE

360 Numerical modelling of RFs variations with back-azimuth at CAN suggests the
361 presence of a complex structure beneath the station, with possibly a dipping fast axis of
362 anisotropy. The fast axis direction is close to the N-S direction in the middle and lower
363 crust (Table 1). This fast axis orientation is roughly parallel to the direction of extension
364 in the Lachlan Orogen and perpendicular to the direction of convergence. The fast axis
365 direction suggests that the observed anisotropy is closely linked to this direction of
366 convergence. The seismic anisotropy could be related to contraction events in the
367 eastern Lachlan Orogen, which occurred at several periods (at least five) between 450

368 Ma and 350 Ma (e.g. Collins 2002b). North-south shortening (generally < 5%) was
369 interactive with east-west shortening during the Lachlan Orogen evolution (e.g. Gray &
370 Foster 2004). However, regional structural relationships between north-south and east-
371 west shortening suggest that the major north-south structural grain of the Lachlan
372 Orogen results from overall east-west shortening (e.g. Gray & Foster 2004). The
373 anisotropy could be due to a strong N-S structural trend in the eastern Lachlan Orogen,
374 which extends from surface to Moho with a variable dip (e.g. Foster & Gray 2000; Gray
375 & Foster 2004) and possibly to the preferred crystallographic orientation of seismically
376 anisotropic minerals in the middle and lower crust (e.g. Siegesmund et al. 1989; Kern &
377 Wenk 1990; Barruol & Kern 1996, Weiss et al. 1999). Previous seismic reflection
378 profiles show indications of an anisotropic upper, middle and lower crust (Direen et al.
379 2001; Glen et al. 2002). Here we clearly identify at CAN seismic anisotropy in the crust
380 from receiver functions.

381 From measurements of *P*-wave polarisation (*Ppol*) at CAN, Fontaine et al. (2009)
382 proposed the presence of a dipping intra-crustal discontinuity. *Ppol* measures the
383 horizontal component of the angle by which *P*-wave polarization deviates from the
384 great-circle path between the source and the receiver. This deviation could be arise
385 from: i) sensor misorientation, ii) a dipping seismic discontinuity, iii) the presence of
386 anisotropy, and iv) velocity heterogeneities beneath the receiver. The estimate of the
387 direction of the fast axis of anisotropy at CAN made from *P*-wave polarisation by
388 Schulte-Pelkum et al. (2001) is -16.47° (i.e 343.53°) and by Fontaine et al. (2009) -
389 12.29° (i.e 347.71°). These directions are close to the fast axis orientations obtained in
390 the lower anisotropic layer (Table 3) from the modelling of the observed radial and
391 transverse RFs variations with back-azimuth. Fontaine et al. (2009) was able to obtain a

392 good fit using a single isotropic layer model and Snell's Law with a dipping seismic
393 discontinuity in the crust to fit the *Ppol* measurements instead of using more complexity
394 with multiple layers. However, the pattern of *Ppol* deviations reported in Fontaine et al.
395 (2009) is also compatible with a fast axis of symmetry azimuth of ca. 330° beneath
396 CAN because a tilt of the axis of hexagonal symmetry away from the horizontal breaks
397 down the 180° periodicity (Schulte-Pelkum et al. 2001). The orientation of 330° is not
398 far from the fast axis azimuth obtained in the lower anisotropic layer with the *P* receiver
399 functions: between 309° and 352° (Table 3).

400 Our results suggests the presence of dipping fast axis of symmetry in the middle and
401 lower crust beneath CAN and may explain the apparent isotropy observed in the
402 analysis of *SKS* splitting at CAN station assuming a horizontal orientation of anisotropy
403 (e.g. Vinnik et al. 1989; Barruol & Hoffmann 1999; Heintz & Kennett 2005).
404 Interestingly, Heintz and Kennett (2005) observed from 3 shear-wave splitting
405 measurements a fast axis azimuth between 22° and 55° at CNB with a delay time in the
406 range 0.5-0.95 s. They commented on the meaning of such a rapid change in elastic
407 properties in the vicinity of Canberra, on a scale of a few tens of kilometres. Due to our
408 limited back-azimuthal resolution at CNB we cannot constrain such a change. However,
409 we do observe clear variations of the RFs on the transverse components between YNG
410 and CAN. The presence of lateral heterogeneities beneath CAN may explain the
411 apparent isotropy observed with splitting measurements at CAN station. The variation
412 of the observed fast axis direction for two different back-azimuths at CNB station
413 (Heintz & Kennett 2005) with good quality splitting measurements may be due to the
414 presence of multiple layers of anisotropy beneath this station.

415 5. Conclusion

416 We have modelled teleseismic RFs using 3 different methods (H-K stacking; non-
417 linear inversion of RFs using NA, and modelling of variations in RFs with back-
418 azimuth) and we were able to confirm several crustal features of the Lachlan Orogen
419 already identified from previous seismic refraction (Finlayson et al. 2002) and reflection
420 profiles (Direen et al. 2001; Glen et al. 2002). The crust-mantle boundary is deep and
421 mostly intermediate in character in the Lachlan Orogen and could arise from
422 underplating at the base of the lower crust and the thick piles of Ordovician mafic rocks
423 present in the mid and lower crust (Glen et al. 2002). Moho depth variations suggest a
424 dipping Moho beneath the Lachlan Orogen. Moreover, numerical modelling of RFs
425 suggests the presence of a dipping Moho and crustal anisotropy with a dipping fast axis
426 beneath CAN (at Mount Stromlo). The cause of crustal anisotropy might be due to a
427 strong N-S structural trend in the eastern Lachlan Orogen, which extends from surface
428 to Moho with a variable dip (e.g. Foster & Gray 2000) and possibly to the preferred
429 crystallographic orientation of minerals in the middle and lower crust caused by palaeo-
430 Pacific plate convergence, which might also give rise to the dipping Moho and crustal
431 thickening to the west beneath CAN station. This crustal thickening may also be related
432 to the broad Macquarie volcanic arc, which is rooted to the Moho.

433 However, it is difficult to distinguish between a dipping seismic discontinuity and
434 the effect of crustal anisotropy with a dipping fast axis on receiver functions. The
435 complexity of the results for a very high-quality permanent station CAN indicates the
436 difficulties we face when we have probes with a limited directional resolution. Where
437 receiver functions can be combined with other classes of information from, e.g.,

438 geological information, surface waves, it may be possible to resolve some of the
439 ambiguities.

440 We confirm a thickened crust beneath the Lachlan orogeny with complex fabric and
441 rapid changes in crustal properties. The presence of a group of high-quality stations
442 enables us to pick up the dip of the Moho and recognise features that seem to have been
443 induced in the compression associated with the construction of the Orogen, including
444 the presence of crustal anisotropy.

445 **Acknowledgments**

446 We thank M. S. Sambridge for his inversion program, A. Frederiksen & M. Bostock
447 for the code to compute synthetic seismograms in anisotropic media. We are grateful to
448 Nick Direen for constructive review. We would also like to thank members of the RSES
449 group for help in the fieldwork deployments, and to the landowners for their support.
450 We are grateful to the developers of GMT software (Wessel & Smith 1991). CAN
451 station is maintained by GEOSCOPE (IPGP) and the Australian National University.
452 CNB and YNG are maintained by Geoscience Australia.

453 **References**

- 454 BANNISTER S., YU J., LEITNER B. & KENNETT B. L. N., 2003. Variations in
455 crustal structure across the transition from West to East Antarctica, Southern Victoria
456 Land. *Geophys. J. Int.* **155**, 870-884.
- 457 BARRUOL G. & HOFFMANN R. 1999. Seismic anisotropy beneath the Geoscope
458 stations from SKS splitting. *Journal of Geophysical Research* **104**, 10 757-10 774.
- 459 BARRUOL G. & KERN H. 1996. Seismic anisotropy and shear-wave splitting in
460 lower-crustal and upper-mantle rocks from the Ivrea Zone – Experimental and
461 calculated data. *Physics of the Earth and Planetary Interiors* **95**, 175-194.

- 462 CHEVROT S. & VAN DER HILST R. D. 2000. The Poisson ratio of the Australian
463 crust: geological and geophysical implications. *Earth and Planetary Science Letters*
464 **183**, 121-132.
- 465 CHRISTENSEN N. I. 1996. Poisson's ratio and crustal seismology. *Journal of*
466 *Geophysical Research* **101**, 3139-3156.
- 467 CLITHEROE G. M., GUDMUNDSSON O. & KENNETT B. L. N. 2000. The crustal
468 thickness of Australia. *Journal of Geophysical Research* **105**, 13697-13713.
- 469 COLLINS C. D. N., DRUMMOND B. J. & NICOLL M. G. 2003. Crustal thickness
470 patterns in the Australian continent. *Geological Society of Australia Special*
471 *Publication* **22**, and *Geological Society of America Special Papers* **372**, 121-128.
- 472 COLLINS C. D. N. 1991. The nature of the crust-mantle boundary under Australia from
473 seismic evidence. In: B.J. Drummond (Editor). *The Australian Lithosphere.*
474 *Geological Society of Australia Special Publication* **17**, 67-80.
- 475 COLLINS W. J. 2002a. Hot orogens, tectonic switching, and creation of continental
476 crust. *Geology* **30**, 535-538.
- 477 COLLINS W. J. 2002b. Nature of extensional accretionary origins. *Tectonics* **21**, 1024-
478 1036.
- 479 CRAMPIN S. 1994. The fracture criticality of crustal rocks. *Geophys. J. Int.* **118**, 428-
480 438.
- 481 CULL J. P., O'REILLY S. Y. & GRIFFIN W. L. 1991. Xenolith geotherms and crustal
482 models in eastern Australia. *Tectonophysics* **192**, 359-366.
- 483 DIREEN N. G. & CRAWFORD A. J. 2003. The Tasman Line: where is it, what is it, is
484 it Australia's Rodinian breakup boundary? *Australian Journal of Earth Sciences* **50**,
485 491-502.

- 486 DIREEN N. G., LYONS P., KORSCH R. J. & GLEN R. A., 2001. Integrated
487 geophysical appraisal of crustal architecture in the eastern Lachlan Orogen.
488 *Exploration Geophysics* **32**, 252–262.
- 489 DRUMMOND B. J. & COLLINS C. D. N. 1986. Seismic evidence for underplating of
490 the lower continental crust of Australia. *Earth and Planetary Science Letters* **79**, 361-
491 372.
- 492 FARRA V., VINNIK L. P., ROMANOWICZ B., KOSAREV G. L. & KIND R. 1991.
493 Inversion of teleseismic S particle motion for azimuthal anisotropy in the upper
494 mantle: a feasibility study. *Geophysical Journal International* **106**, 421-431.
- 495 FINLAYSON D. M., KORSCH R. J., GLEN R. A., LEVEN J. H. & JOHNSTONE D.
496 W. 2002. Seismic imaging and crustal architecture across the Lachlan Transverse
497 Zone, a crosscutting feature of eastern Australia. *Australian Journal of Earth
498 Sciences* **49**, 311–321.
- 499 FINLAYSON D. M., COLLINS C. D. N. & DENHAM D. 1980. Crustal structure
500 under the Lachlan Fold Belt, southeastern Australia. *Physics of the Earth and
501 Planetary Interiors* **21**, 321-342.
- 502 FONTAINE F. R., TKALCIC H. & KENNETT B. L. N. 2013. Imaging crustal
503 structure variation across southeastern Australia. *Tectonophysics* **582**, 112-125.
- 504 FONTAINE F. R., BARRUOL G., KENNETT B. L. N., BOKELMANN G. &
505 REYMOND D. 2009. Upper mantle anisotropy beneath Australia and Tahiti from P-
506 wave polarization - Implications for real-time earthquake location. *Journal of
507 Geophysical Research* **114**, B03306, doi:10.1029/2008JB005709.
- 508 FOSTER D. A. & GRAY D. R. 2000, Evolution and structure of the Lachlan Fold Belt
509 (Orogen) of Eastern Australia. *Ann. Rev. Earth Planet. Sci.* **28**, 47-80.

- 510 FREDERIKSEN A. W., FOLSOM H. & ZANDT G. 2003. Neighbourhood inversion of
511 teleseismic Ps conversions for anisotropy and layer dip. *Geophys. J. Int.* **155**, 200-
512 212.
- 513 FREDERIKSEN A. W. & BOSTOCK M. G. 2000. Modelling teleseismic waves in
514 dipping anisotropic structures. *Geophysical Journal International* **141**, 401-412.
- 515 GIESE P. 2005. Moho discontinuity. In: Selly R. C., Cocks L. R. M. & Plimer I. R.
516 eds., *Encyclopedia of Geology*, pp 645-659 Elsevier Academic Press, Oxford.
- 517 GLEN R. A., KORSCH R. J., DIREEN N. G., JONES L. E. A., JOHNSTONE D. W.,
518 LAWRIE K. C., FINLAYSON D. M. & SHAW R. D. 2002. Crustal structure of the
519 Ordovician Macquarie Arc, eastern Lachlan Orogen, based on seismic-reflection
520 profiling. *Australian Journal of Earth Sciences* **49**, 323-348.
- 521 GRAY D. R. & FOSTER D. A. 2004. Tectonic evolution of the Lachlan Orogen,
522 southeast Australia: historical review, data synthesis and modern perspectives.
523 *Australian Journal of Earth Sciences* **51**, 773-817.
- 524 HASKELL N. A. 1953. The dispersion of surface waves in multilayered media. *Bull.*
525 *Seismol. Soc. Am.* **43**, 17-34.
- 526 HEINTZ M. & KENNETT B. L. N. 2005. Continental scale shear wave splitting
527 analysis: Investigation of seismic anisotropy underneath the Australian continent.
528 *Earth and Planetary Science Letters* **236**, 106-119.
- 529 KENNETT B. L. N., SALMON M., SAYGIN E. & AUSMOHO GROUP 2011.
530 AusMoho: the variation of Moho depth in Australia. *Geophysical Journal*
531 *International* **187**, 946-958.

- 532 KERN H. & WENK H.-R. 1990. Fabric-related velocity anisotropy and shear wave
533 splitting in rocks from the Santa Rosa Mylonite Zone. *J. Geophys. Res.* **95**, 11213-
534 11223.
- 535 LANGSTON C. A. 1979. Structure under Mount Rainier, Washington, inferred from
536 teleseismic body waves. *J. Geophys. Res.* **84**, 4749-4762.
- 537 LANGSTON C. A. 1977. Corvallis, Oregon, crustal and upper mantle structure from
538 teleseismic body waves. *Bull. Seismol. Soc. Am.* **67**, 713-724.
- 539 MCDONOUGH W. F., RUDNICK R. L. & MCCULLOCH M. T. 1991. The chemical
540 and isotopic composition of the lower eastern Australian lithosphere: a review. *In*:
541 Drummond B. J. ed. *The Australian Lithosphere*, pp. 163-188. Geological Society of
542 Australia Special Publication **17**.
- 543 O'REILLY S. Y. 1989. Nature of the Australian lithosphere. *In*: Johnson R. W. ed.
544 *Intraplate Volcanism in Eastern Australia and New Zealand*, pp. 290-297. Cambridge
545 University Press, Cambridge.
- 546 PENG X. & HUMPHREYS E. D. 1997. Moho Dip and Crustal Anisotropy in
547 Northwestern Nevada from Teleseismic Receiver Functions. *Bulletin of the*
548 *Seismological Society of America* **87**, 745-754.
- 549 RAWLINSON N., KENNETT B. L. N., VANACORE E., GLEN R. A. & FISHWICK
550 S. 2010. The structure of the upper mantle beneath the Delamerian and Lachlan
551 orogens from simultaneous inversion of multiple teleseismic datasets. *Gondwana*
552 *Research* **19**, 788-799.
- 553 SAMBRIDGE M. S. 1999. Geophysical inversion with a neighbourhood algorithm. I.
554 Searching a parameter space. *Geophysical Journal International* **138**, 479-494.

- 555 SAVAGE M. K. 1998. Lower crustal anisotropy or dipping boundaries ? Effects on
556 receiver functions and a case study in New Zealand. *Journal of Geophysical Research*
557 **103**, 15 069-15 087.
- 558 SAYGIN E. 2007. Seismic receiver and noise correlation based studies in Australia.
559 Ph.D. thesis, The Australian National University, Canberra, 175p. (unpubl.).
- 560 SCHULTE-PELKUM V., MASTERS G. & SHEARER P. M. 2001. Upper mantle
561 anisotropy from long-period P polarization. *Journal of Geophysical Research* **106**, 21
562 917-21 934.
- 563 SHERRINGTON H. F., ZANDT G. & FREDERIKSEN A. 2004. Crustal fabric in the
564 Tibetan Plateau based on waveform inversions for seismic anisotropy parameters.
565 *Journal of Geophysical Research* **109**, B02312, doi:10.1029/2002JB002345.
- 566 SHIBUTANI T., SAMBRIDGE M. S. & KENNETT B. L. N. 1996. Genetic algorithm
567 inversion for receiver functions with application to crust and uppermost mantle
568 structure beneath Eastern Australia. *Geophys. Res. Lett.* **23**, 1826-1832.
- 569 SIEGESMUND S., TAKESHITA T. & KERN H. 1989. Anisotropy of Vp and Vs in an
570 amphibolite of the deeper crust and its relationship to the mineralogical,
571 microstructural, and textural characteristics of the rock. *Tectonophysics* **157**, 25-38.
- 572 THOMSON W. T. 1950. Transmission of elastic waves through a stratified solid. *J.*
573 *appl. Physics* **21**, 89-93.
- 574 TKALCIC H., CHEN Y., LIU R., HUANG H., SUN L. & CHAN W. 2011. Multi-Step
575 modelling of teleseismic receiver functions combined with constraints from seismic
576 tomography: Crustal structure beneath southeast China. *Geophys. J. Int.* **187**, 303-
577 326.

- 578 VINNIK L. P., FARRA V. & ROMANOWICZ B. 1989. Azimuthal anisotropy in the
 579 Earth from observations of SKS at Geoscope and NARS broadband stations. *Bulletin*
 580 *of the Seismological Society of America* **79**, 1542-1558, 1989.
- 581 WEISS T., SIEGESMUND S., RABELL W., BOHLEN T. & POHL M. 1999. Seismic
 582 velocities and anisotropy of the lower continental crust: A review. *Pure App.*
 583 *Geophys.* **156**, 97-122.
- 584 WESSEL P. & SMITH W. H. 1991. Free software helps map and display data. *Eos*
 585 *Trans., AGU* **72**, 441-446.
- 586 ZHU L. & KANAMORI H. 2000. Moho depth variation in southern California from
 587 teleseismic receiver functions. *Journal of Geophysical Research* **105**, 2969-2980.

588

589 **Figure Captions**

590 **Fig. 1.** a) Location of the 323 events used for receiver functions analysis at station
 591 CAN. The rectangle shows the limits of southeastern Australia and the star represents
 592 the location of CAN station. b) Simplified geological map of southeastern Australia
 593 modified from Gray & Foster (2004) with the location of the SoCP (Southern Cratons to
 594 Palaeozoic) seismic network and the permanent seismic stations from Geoscience
 595 Australia (GA) and GEOSCOPE networks. Key to marked feature: NVP, Newer
 596 Volcanic Province. c) Simplified map of the Lachlan Orogen (modified from Glen et al.
 597 2002 and Finlayson et al. 2002). The three elements of the Ordovician Macquarie Arc
 598 are shown, the Junee-Narromine Volcanic Belt (JNVB), Molong Volcanic Belt (MVB),
 599 Gulong Volcanic Belt (GVB). LTZ is the Lachlan Transverse Zone. Seismic lines show
 600 the location of reflection profiles (Direen et al. 2001; Glen et al. 2002). A and B are the
 601 location of the extremities of the refraction profile from Finlayson et al. (2002).

602 **Fig. 2.** Results from the H-K stacking analysis for RFs (Zhu & Kanamori 2000). a)
603 Stack over 10° epicentral distance intervals of radial RFs at CAN seismic station.
604 Numbers on right side are numbers of RFs stacked for each distance interval. Triangles
605 indicate computed arrival times of phases *Pms* and *PpPms* for the best solution. b)
606 Normalized amplitudes of the stack over all back-azimuths along the travel time curves
607 corresponding to the *Pms* and *PpPms* phases at CAN. Although $H=26$ km and
608 $V_p/V_s=1.58$ correspond to a global maximum, there is also a local maximum in the H-K
609 stack at values that are more physically realistic and more consistent with other
610 modelling methods: $H=39$ km and $V_p/V_s=1.72$. The estimated values of H and V_p/V_s
611 strongly depend on which peak is identified as *Pms* by the stacking method.

612 **Fig. 3.** a) and b) Figure details are as shown as Figures 2a and 2b for station CNB.
613 $H=39$ km and $V_p/V_s=1.70$.

614 **Fig. 4.** a) and b) Figure details are as shown as Figures 2a and 2b for station SO01.
615 $H=39$ km and $V_p/V_s=1.78$.

616 **Fig. 5.** a) and b) Comparison between the observed average and the predicted radial RFs
617 from the NA inversion at SO01 and CAN. c) and d) The 1-D shear wave velocity
618 models obtained from the NA inversion at SO01 and CAN. All the 22 600 models
619 searched in the NA inversion are shown as the gray shaded area. The best 1000 models
620 are shown as a yellow and green area, the colour being logarithmically proportional to
621 the number of models. The colour scale shows the increase in data fit from yellow to
622 green. A dashed red line represents the best data-fitting model. A solid blue line
623 represents the average model of the best 1000 fitting models. 0 km depth corresponds to
624 the station elevation.

625 **Fig. 6.** a) and b) Comparison between the observed average and the predicted radial RFs
626 from the NA inversion at CNB and YNG. c) and d) The 1-D shear wave velocity
627 models obtained from the NA inversion at CNB and YNG. Figure details are as shown
628 as Figures 5a and 5b.

629 **Fig. 7.** a) Radial RFs versus back-azimuth at CAN. b) Transverse RFs versus back-
630 azimuth at CAN. Arrows and circles illustrate delay time and variation of polarity
631 related to dipping and anisotropic effects.

632 **Fig. 8.** a) Comparison between observed average radial RFs at CNB and CAN. The *Pms*
633 phase arrives earlier at CNB suggesting a thinner crust than below CAN. b) Synthesis of
634 1-D shear wave velocity models derived from teleseismic earthquakes near CAN
635 station. The red lines are the average models of the best 100 fitting models derived for
636 each station in the NA inversion. The Moho is interpreted to be the base of the high-
637 velocity gradient zone, shown in black shading. We connected by a dashed line seismic
638 discontinuities, which are similar beneath two adjacent seismic stations. c) Cartoon
639 showing our interpretation of the 1-D shear wave velocity models at CAN and CNB
640 stations. This interpretation is also consistent with observed variations of RFs with
641 back-azimuths at CAN.

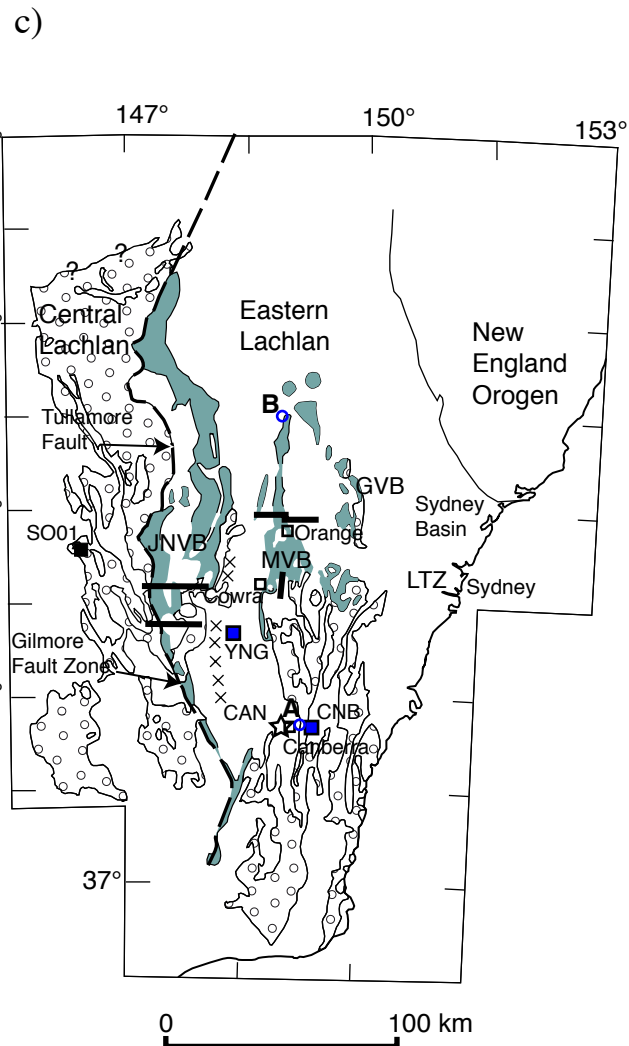
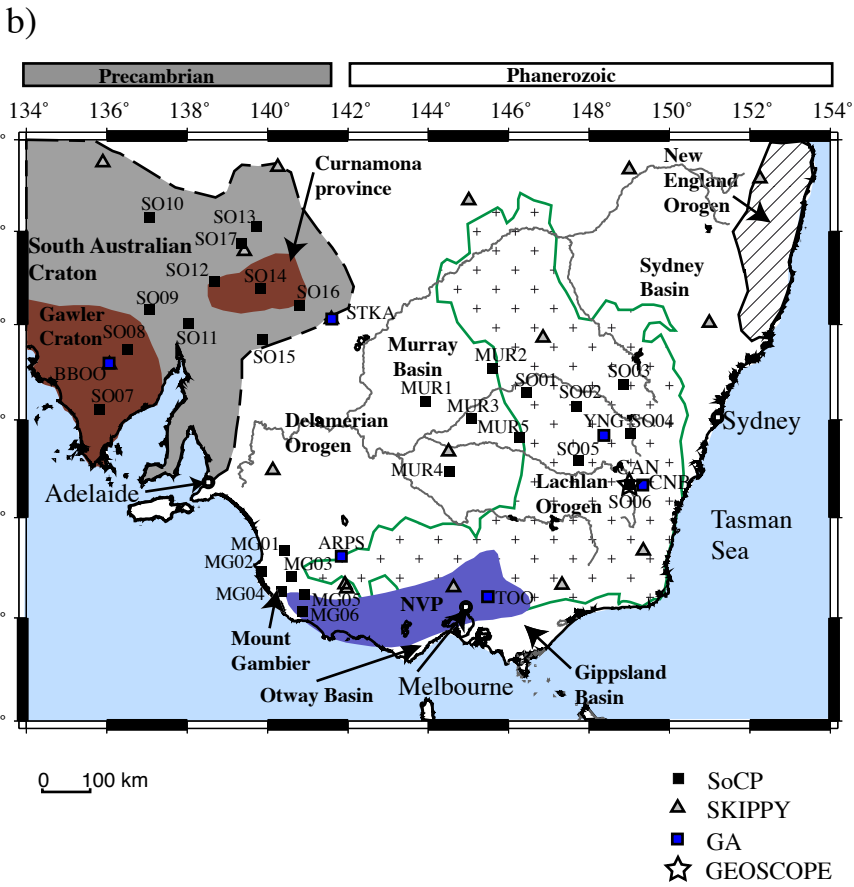
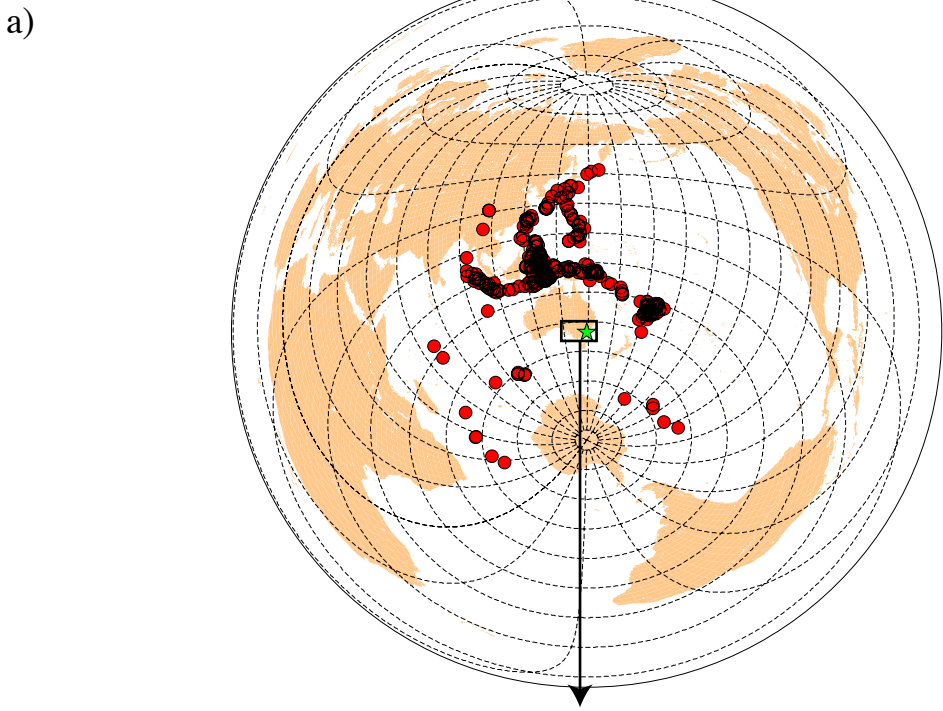
642 **Fig. 9.** Location map of the depth of the crust-mantle seismic discontinuity beneath
643 southeastern Australia. Two different symbols are used: stars represent location and
644 crustal thicknesses from a previous study (Fontaine et al. 2013) and this study (heavier
645 outline). Octagons show results from previous studies (Shibutani et al. 1996; Clitheroe
646 et al. 2000; Collins 1991; Collins et al. 2003; Saygin 2007). b) Simplified tectonic
647 architecture of the Lachlan Orogen (modified from Glen et al. 2002 and Finlayson et al.
648 2002). The three elements of the Ordovician Macquarie Arc are shown, the June-

649 Narromine Volcanic Belt (JNVB), Molong Volcanic Belt (MVB), Gulong Volcanic
650 Belt (GVB). LTZ is the Lachlan Transverse Zone.

651 **Fig. 10.** a) Radial RFs versus back-azimuth at YNG. b) Transverse RFs versus back-
652 azimuth at YNG.

653 **Fig. 11.** a) Radial RFs versus back-azimuth at CNB. b) Transverse RFs versus back-
654 azimuth at CNB.

655 **Fig. 12.** a) Synthetic radial RFs versus back-azimuth at CAN for the best-fitting model
656 (see Table 2). b) Synthetic transverse RFs versus back-azimuth at CAN for the best-
657 fitting model.



- Macquarie Arc
- MORB volcanics
- Craton-derived turbidites
- Seismic reflection lines
- AB** Extremities of recording sites from a wide-angle seismic profile
- Broad-band seismic networks:
- SoCP
- GA
- GEOSCOPE

Figure 1
Fontaine et al. 2013

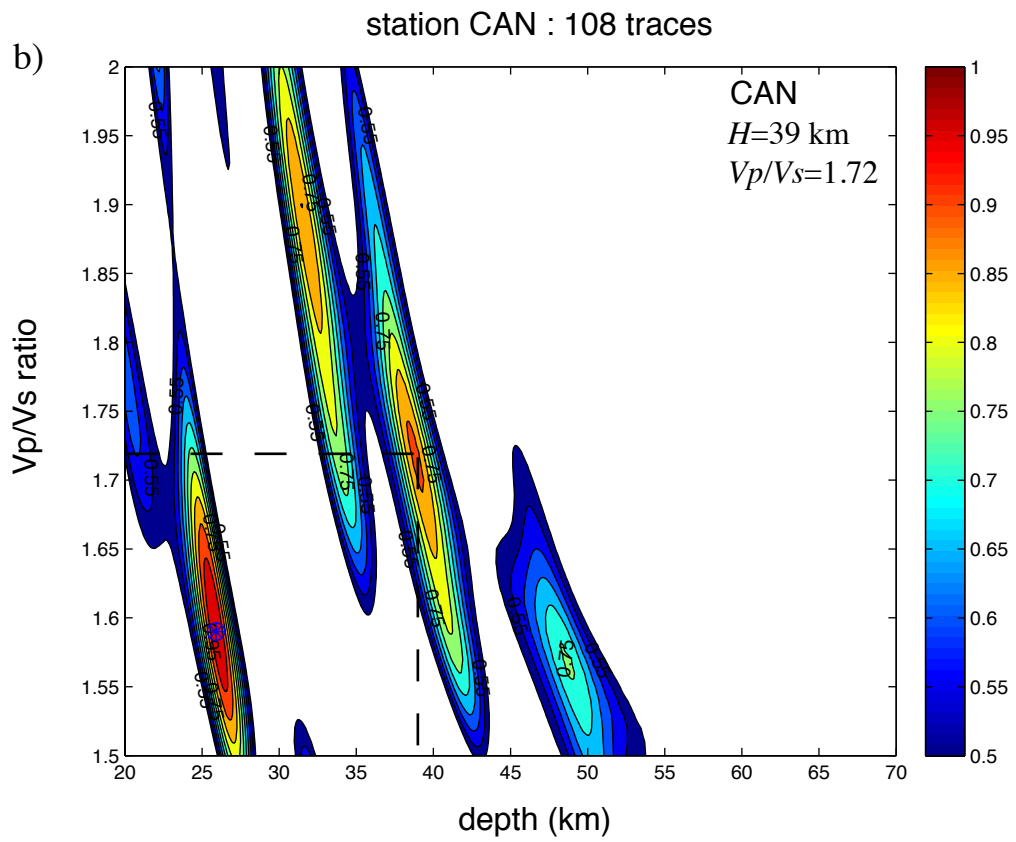
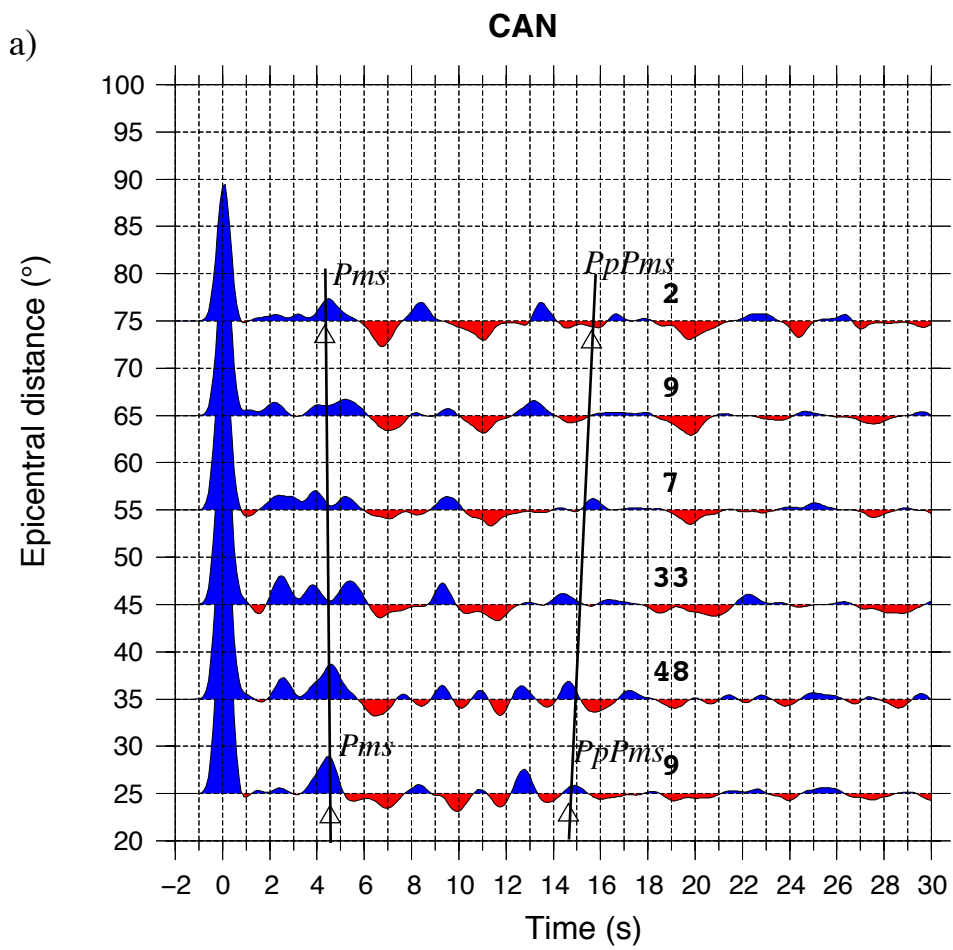
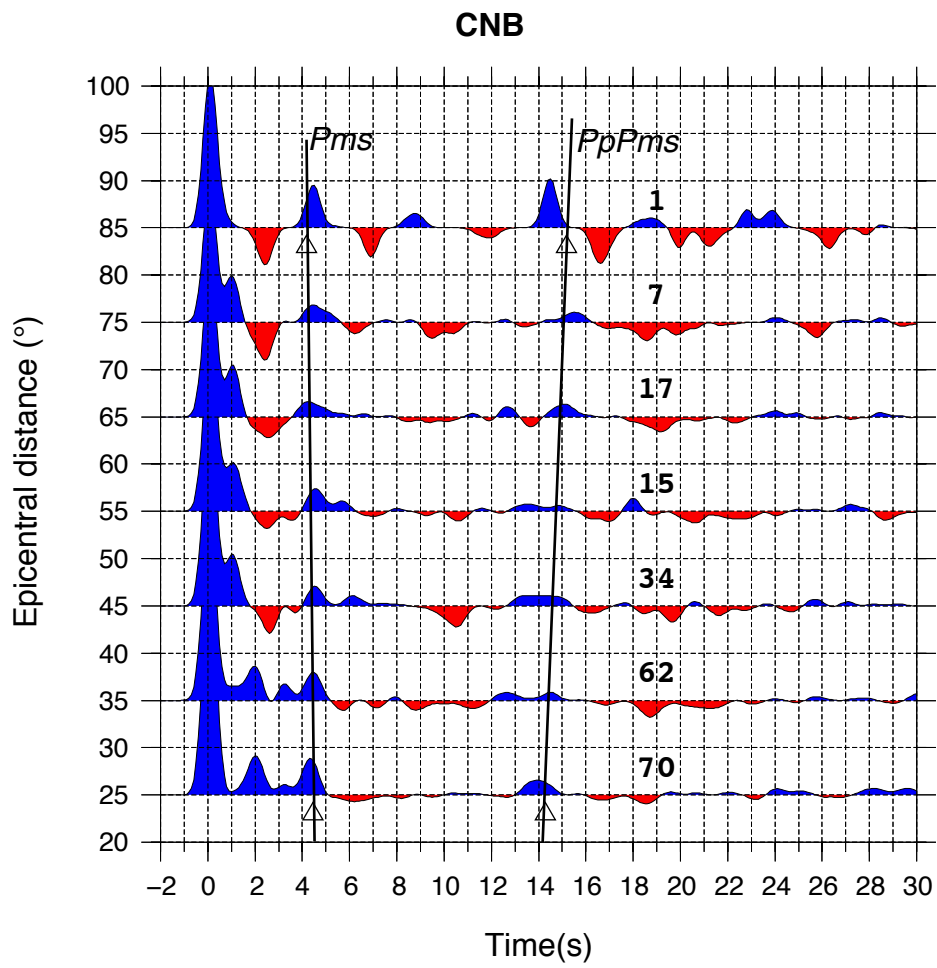


Figure 2
 Fontaine et al. 2013

a)



b)

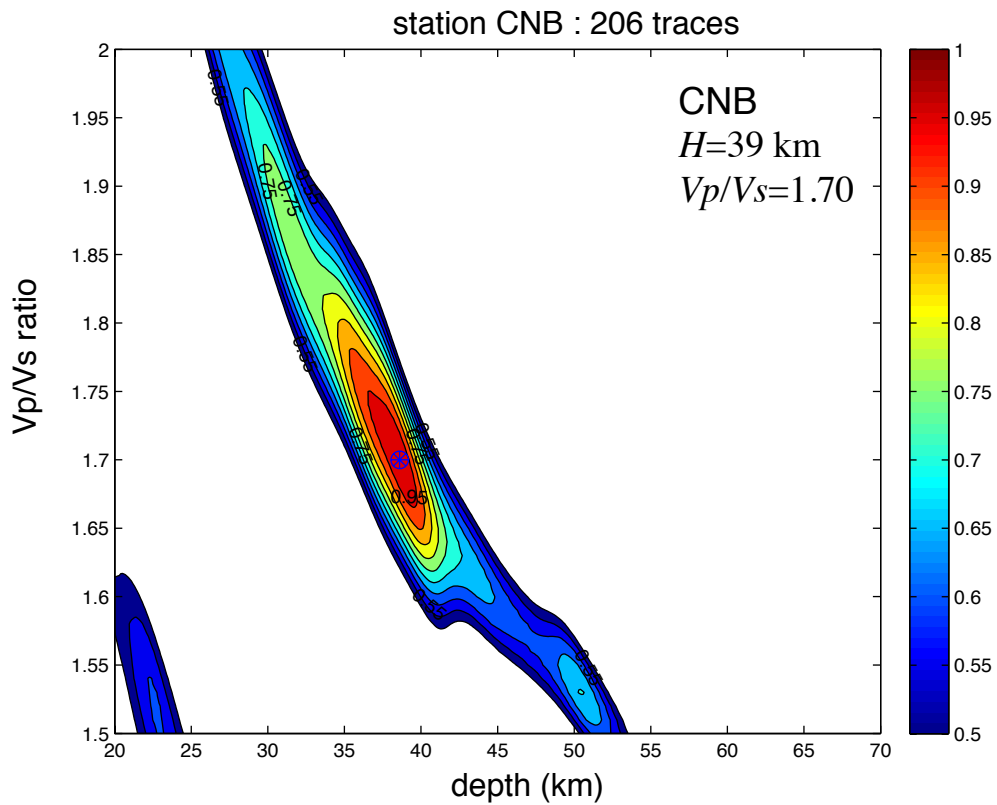


Figure 3
Fontaine et al. 2013

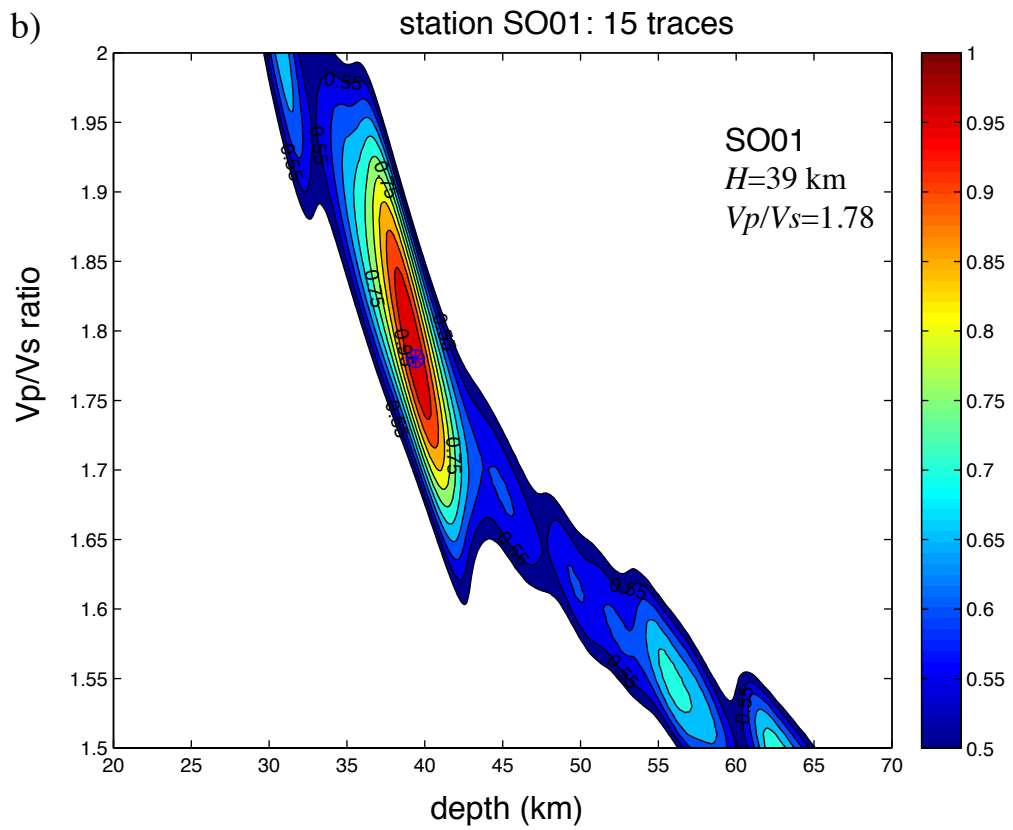
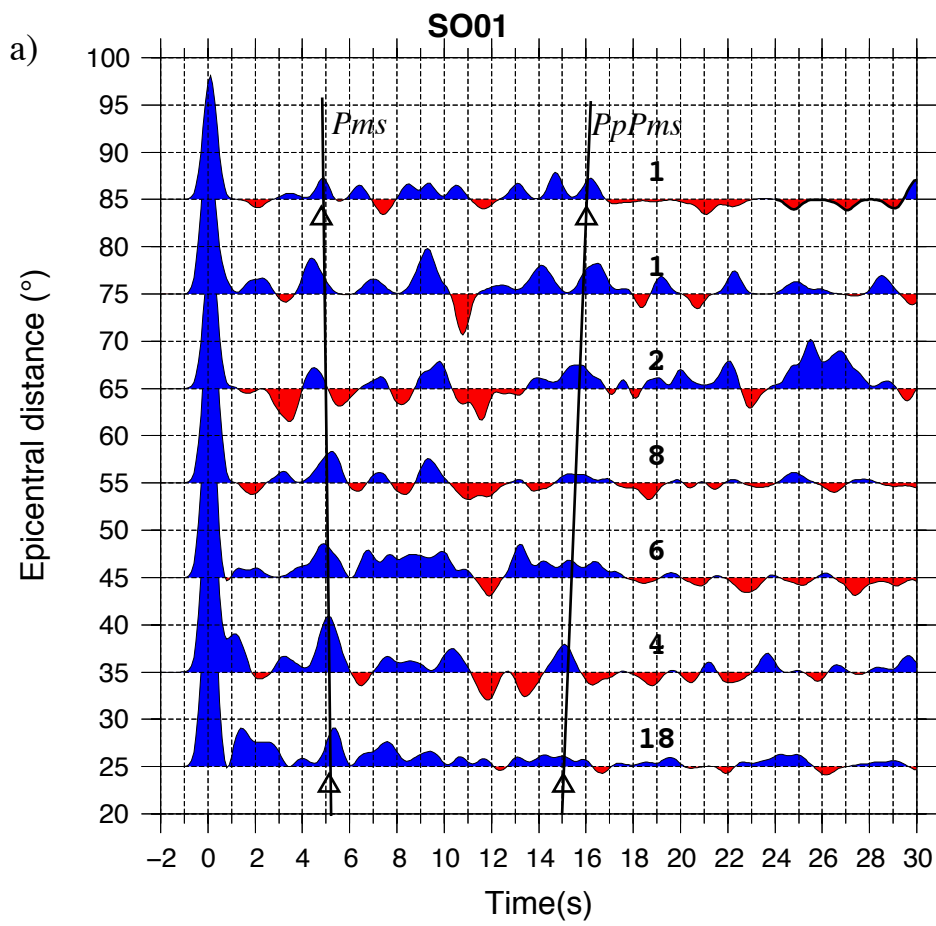


Figure 4
Fontaine et al. 2013

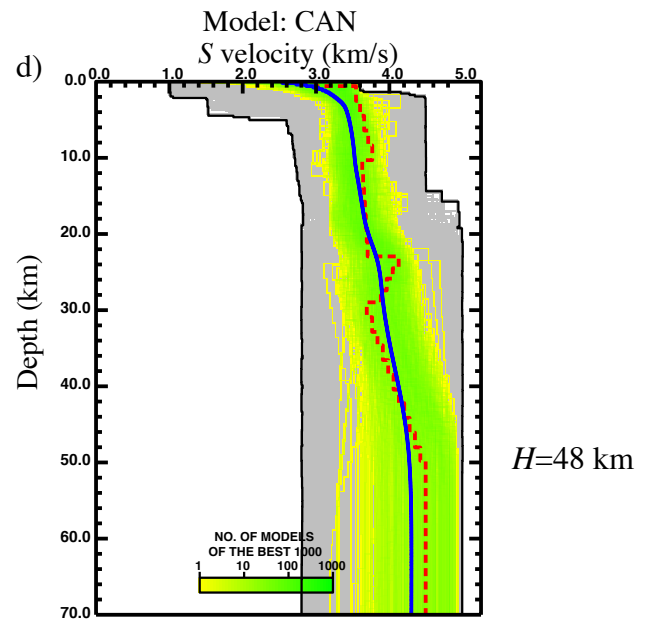
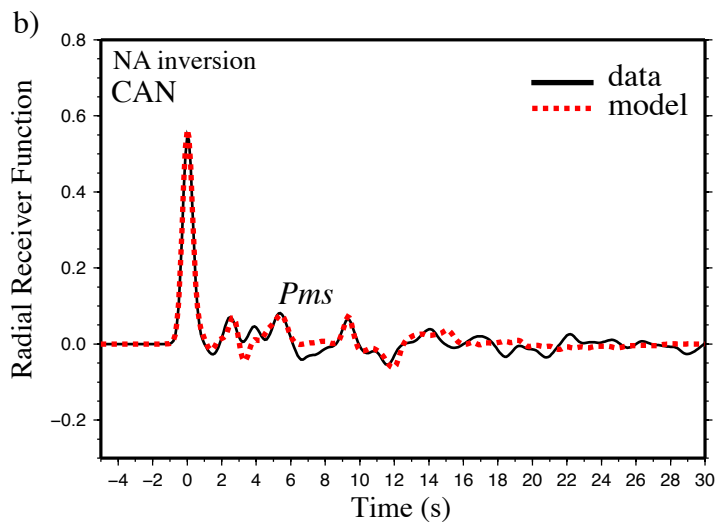
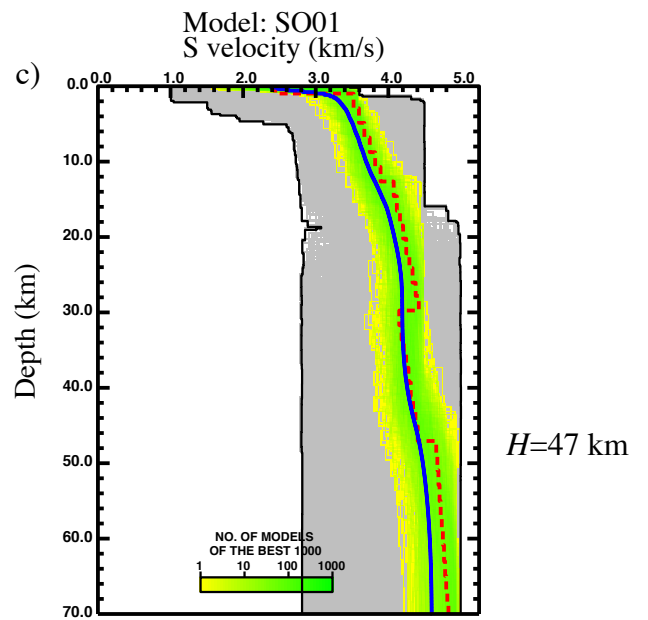
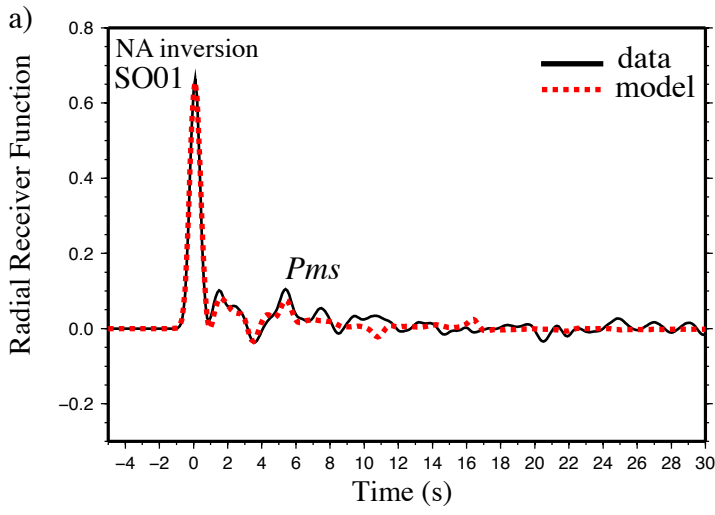


Figure 5
Fontaine et al. 2013

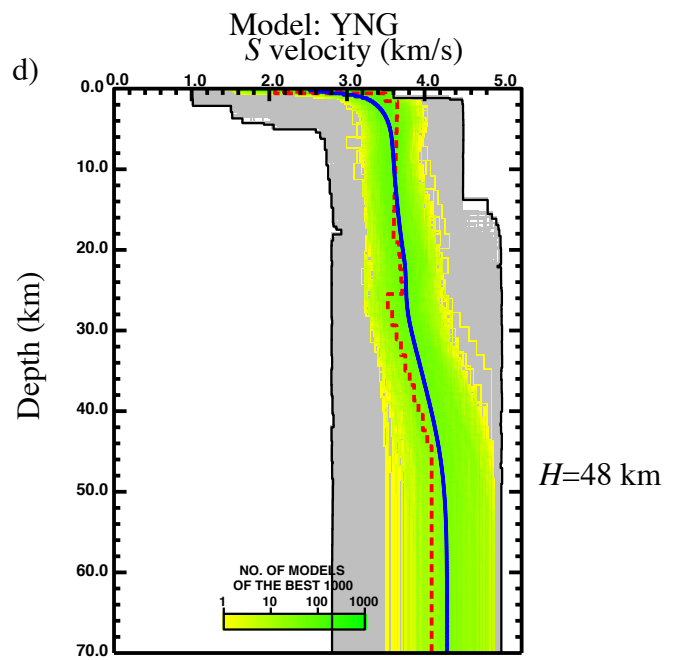
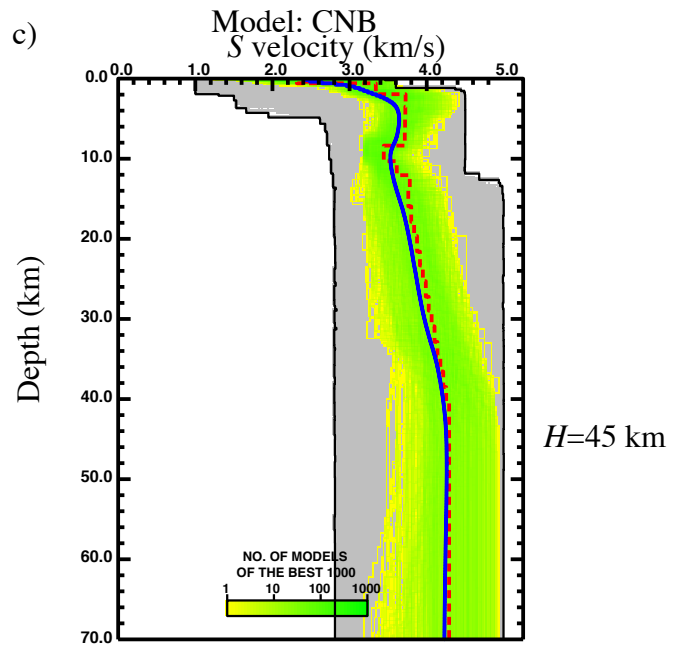
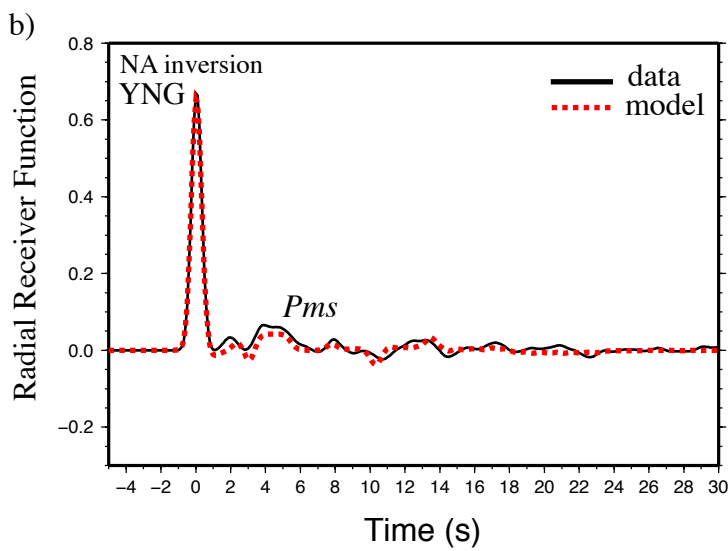
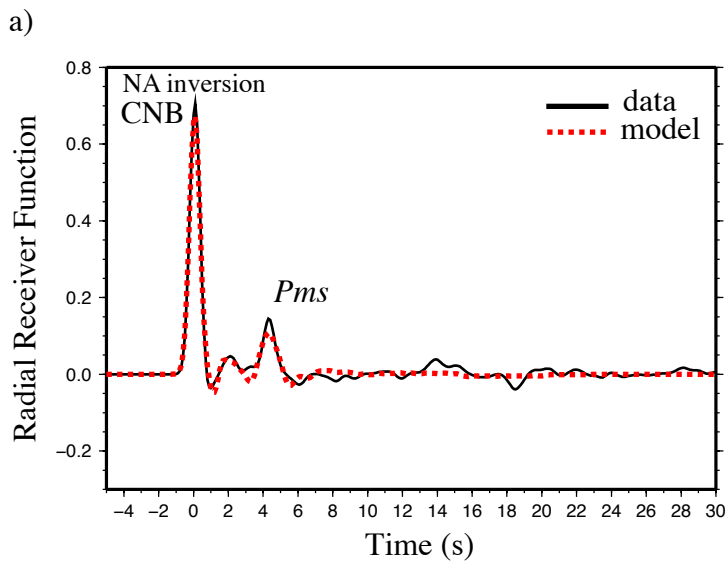


Figure 6
Fontaine et al. 2013

CAN, observed receiver functions

a) Radial

b) Transverse

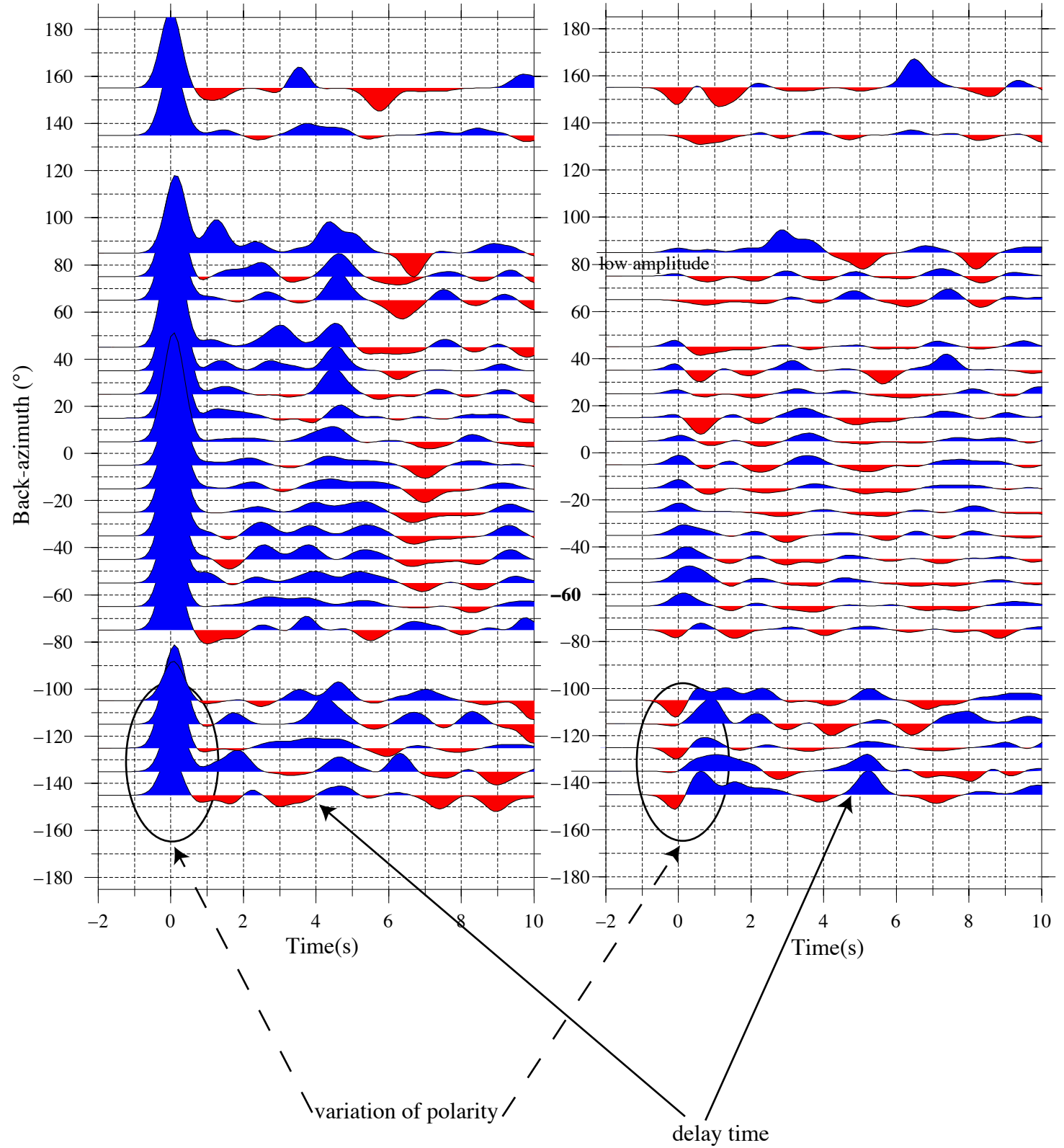
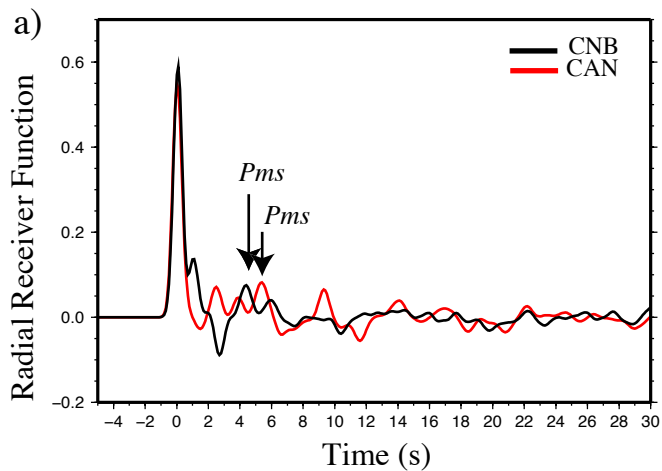


Figure 7
Fontaine et al. 2013



b) NA inversion

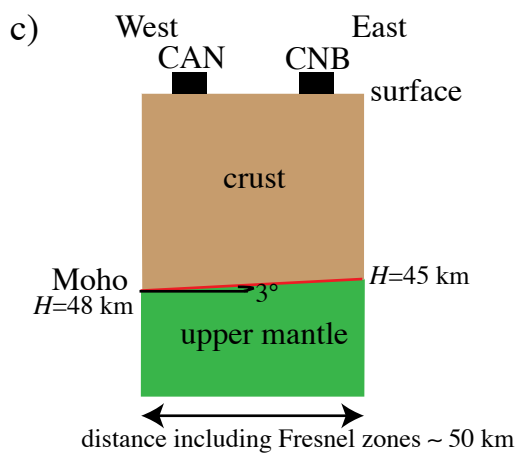
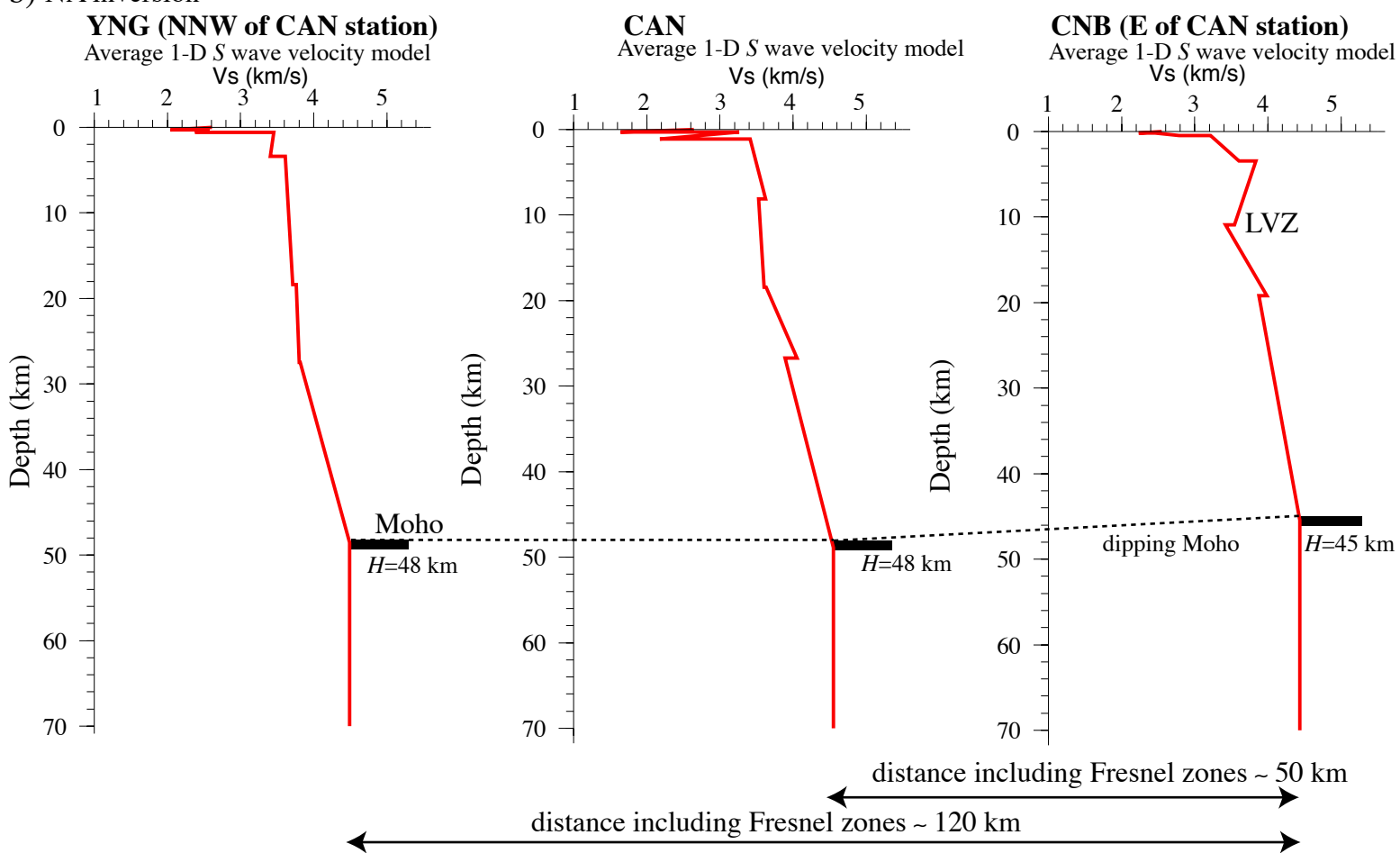
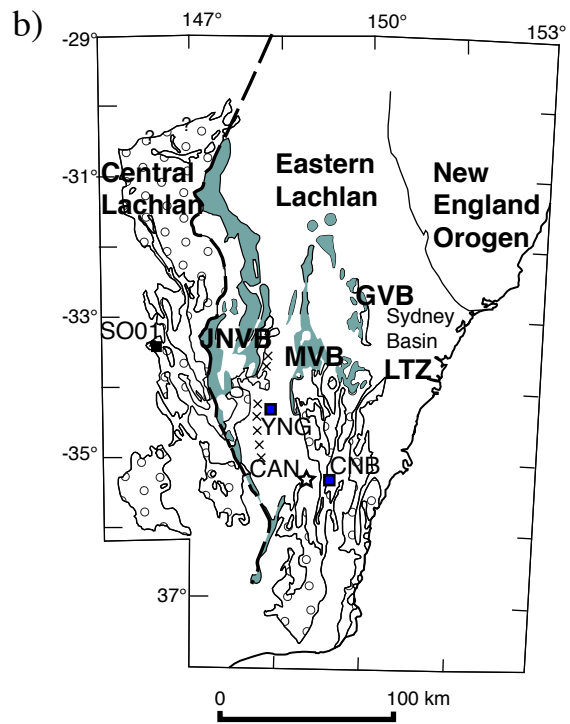
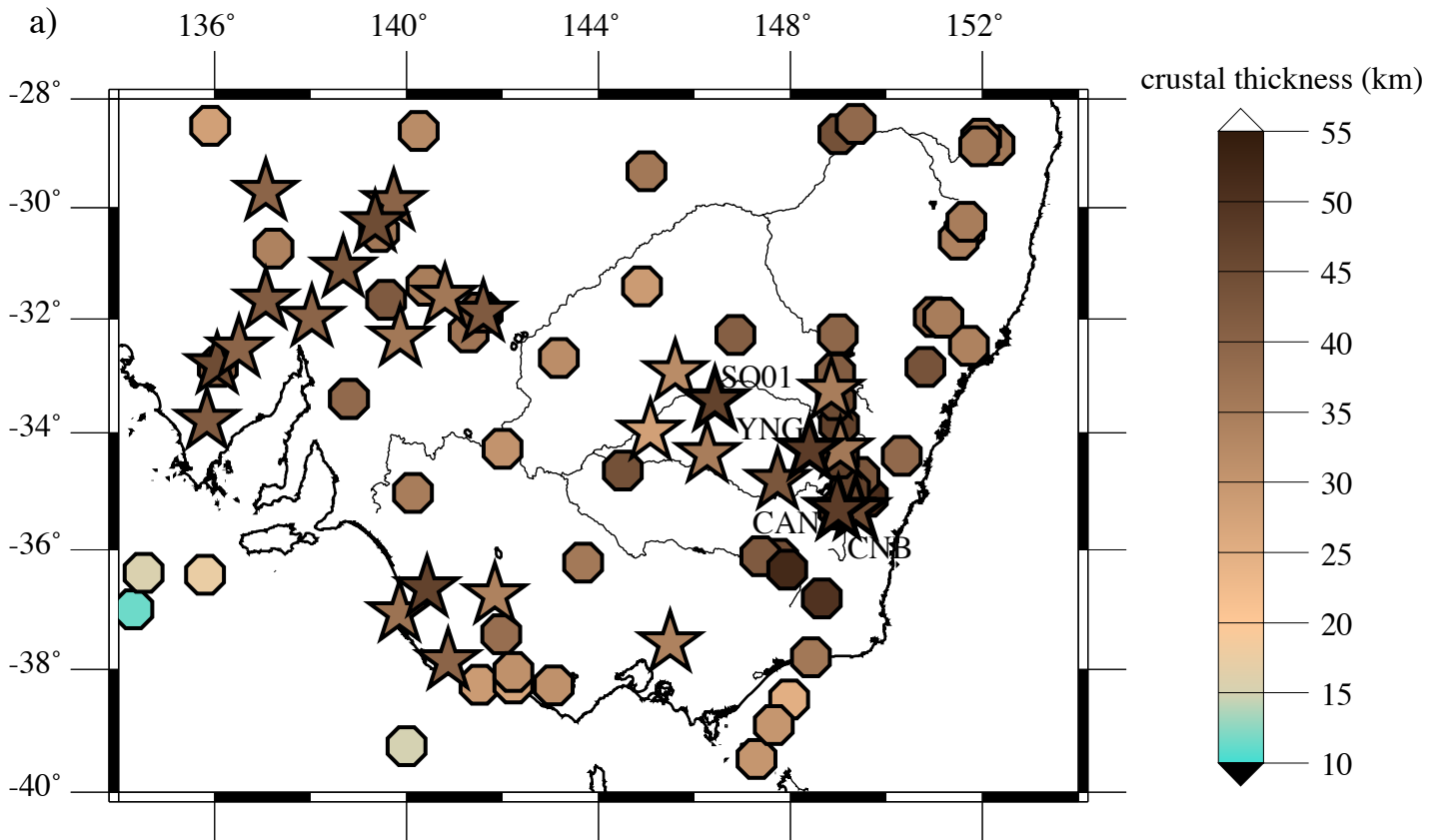


Figure 8
Fontaine et al. 2013



- Macquarie Arc
 - MORB volcanics
 - Craton-derived turbidites
- Broad-band seismic networks:
- SoCP
 - GA
 - GEOSCOPE

Figure 9
Fontaine et al. 2013

YNG, observed receiver functions

a) Radial

b) Transverse

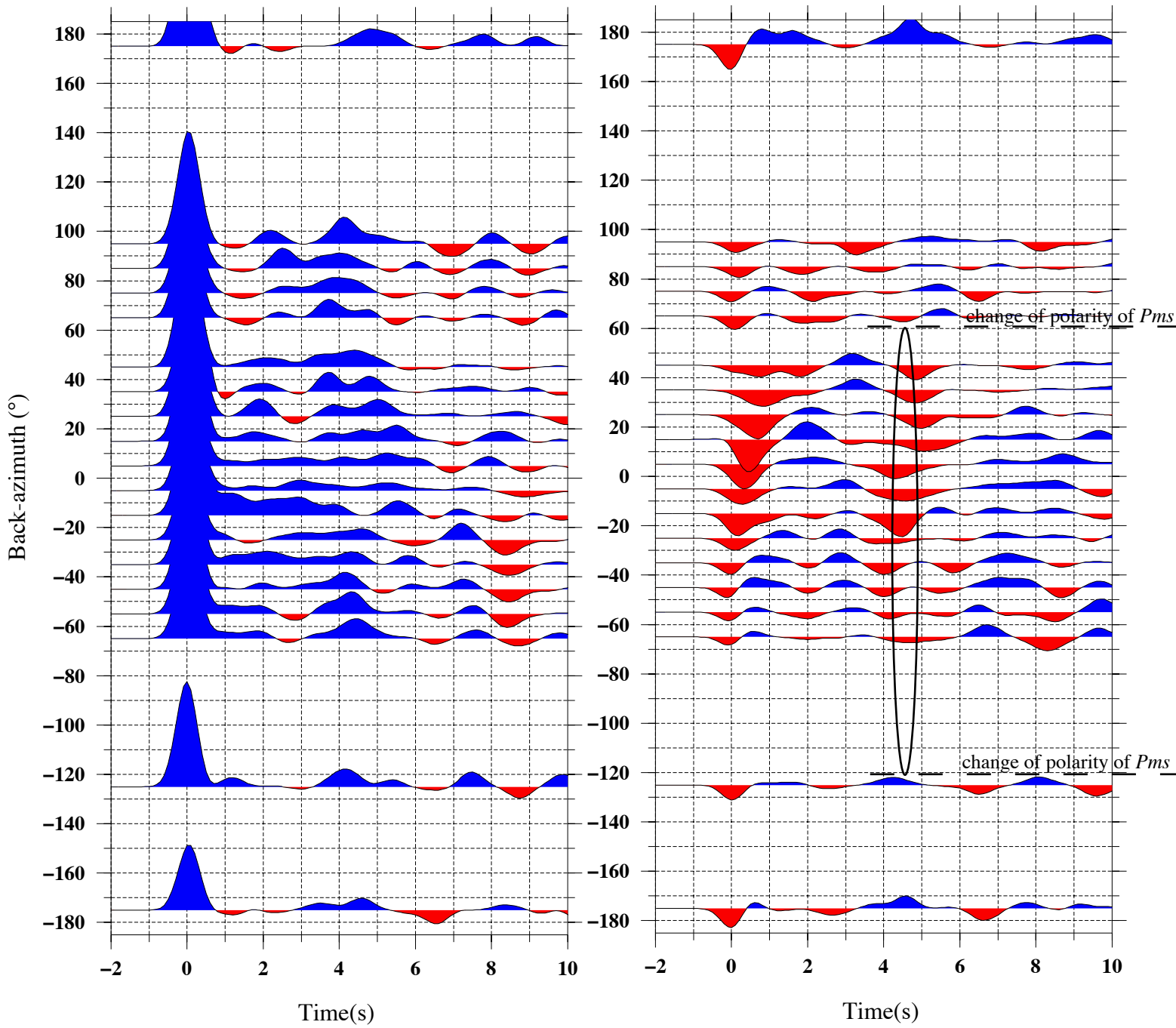
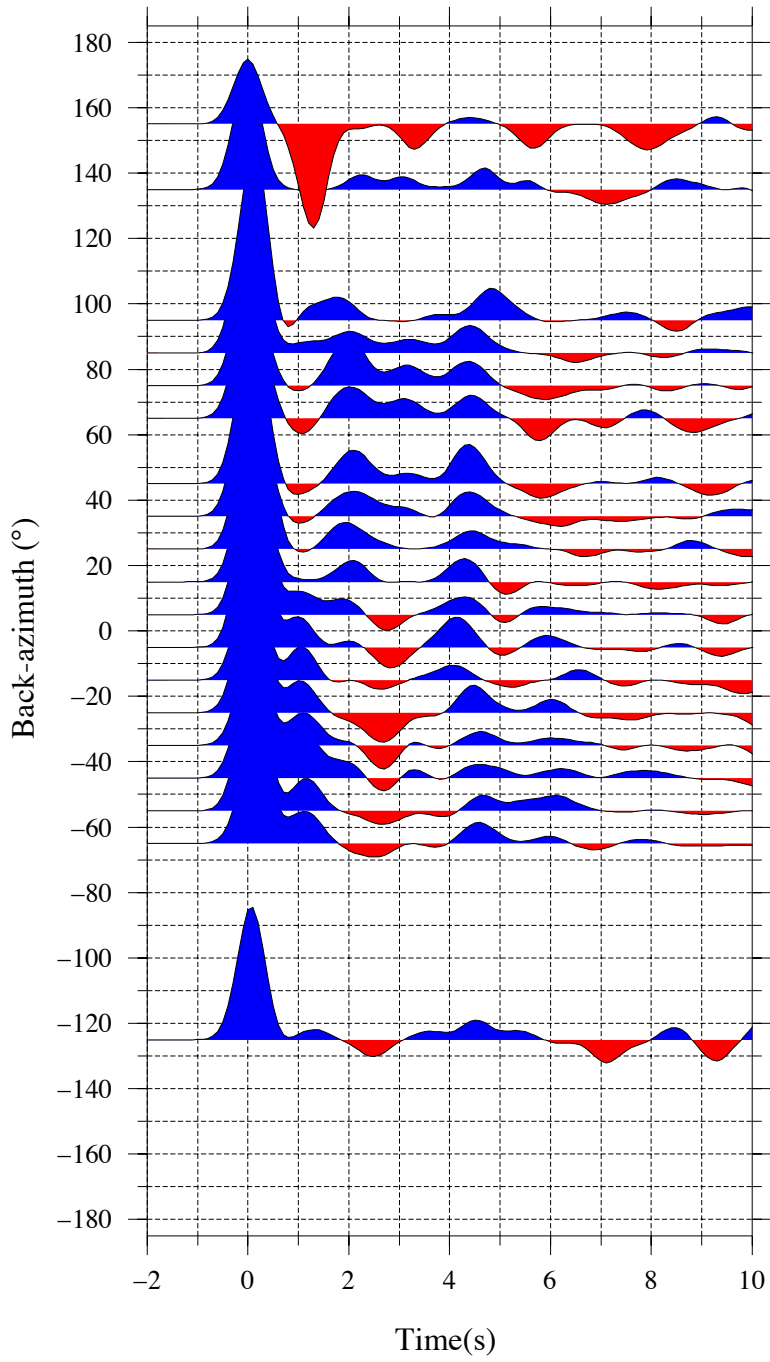


Figure 10
Fontaine et al. 2013

CNB, observed receiver functions

a) Radial



b) Transverse

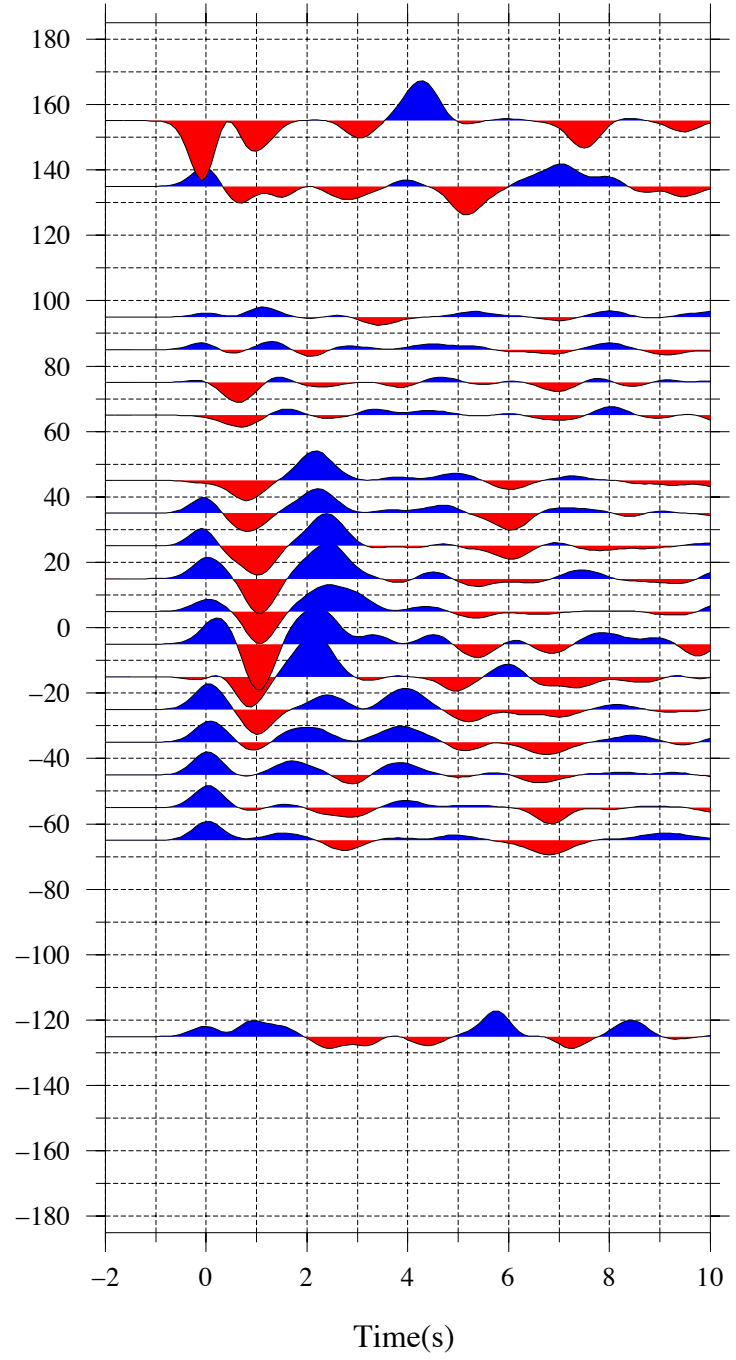
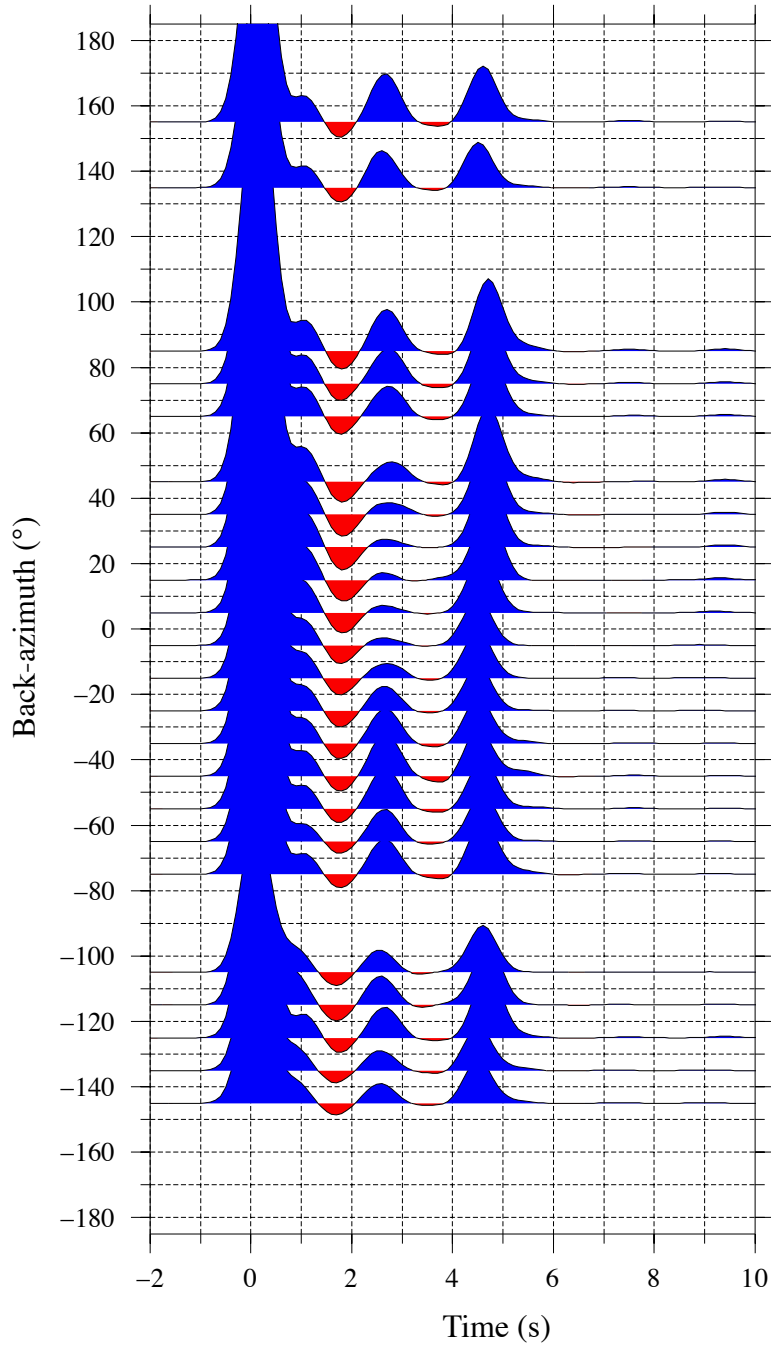


Figure 11
Fontaine et al. 2013

Model: CAN, synthetics

a) Radial



b) Transverse

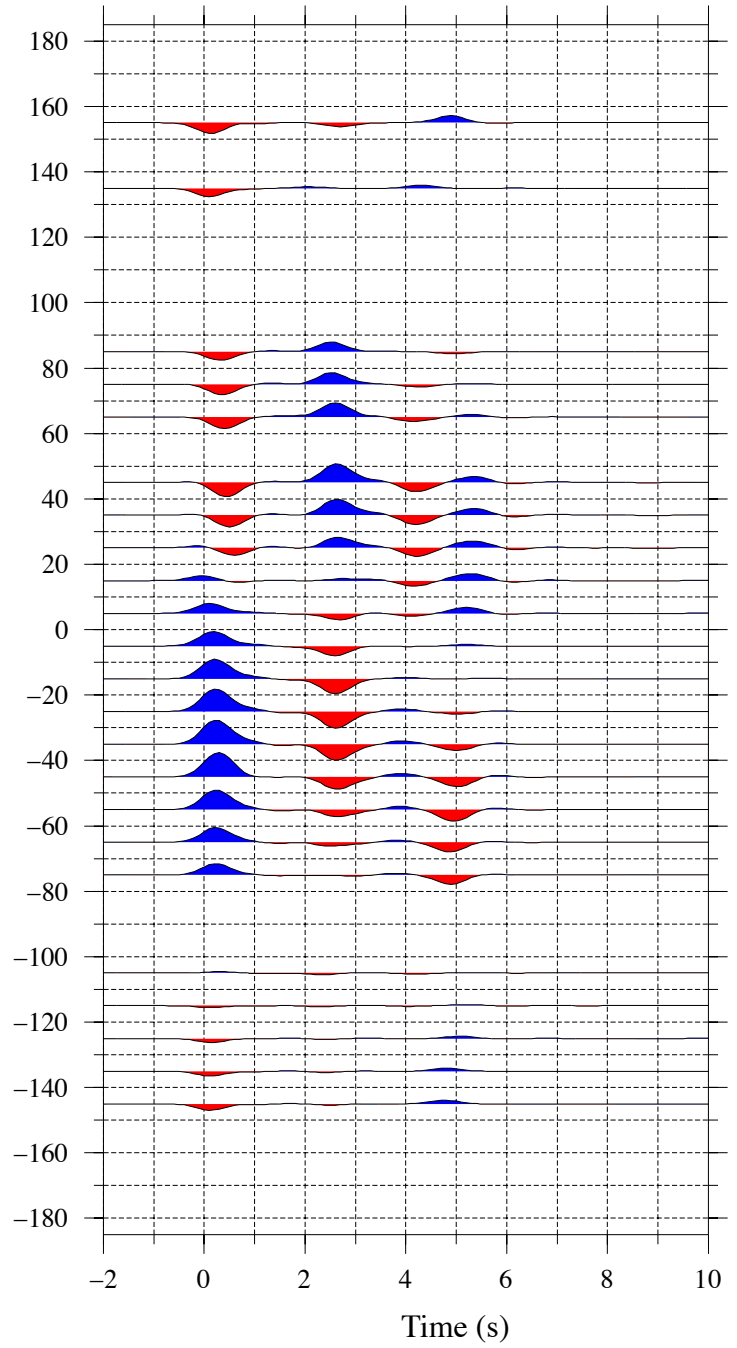


Figure 12
Fontaine et al. 2013

Table 1. Average anisotropic model of the best 100 models generated during the neighbourhood inversion of radial and transverse receiver functions at CAN. 20 parameters (in bold) were searched during the inversion. The remaining parameters are fixed from previous studies constraints (Finlayson et al. 2002; Glen et al. 2002). Layers are listed from top to bottom. Strike and dip refer to the upper interface of the layer. The down-dip direction is 90° clockwise of strike. $\langle V_S \rangle$ and $\langle V_P \rangle$ are average S -wave and P -wave velocities. Azimuth is the direction of the fast axis (in degrees). Pl is the plunge of the fast axis. P anis. and S anis. are the percentage anisotropy for P and S wave; the remaining parameter η is fixed at 1.03 (Farra et al. 1991; Frederiksen & Bostock 2000).

Thickness	ρ	$\langle V_P \rangle$	$\langle V_S \rangle$	P	S	Azimuth	Pl	Strike	Dip
(km)	(g/cm ³)	(km/s)	(km/s)	anis.	anis.	(°)	(°)	(°)	(°)
1.76	2.625	5.550	2.640	0	0	N/A	N/A	0	0
19.00	2.612	6.163	3.620	6.0	0.3	6	21	0	0
26.00	2.652	6.105	3.997	9.9	0.3	327	3	0	0
half-space	3.223	8.214	4.582	0	0	N/A	N/A	172	3

Table 2. Parameters from the best model of the 18000 models generated during the neighbourhood inversion of radial and transverse receiver functions at CAN station.

Thickness	ρ	$\langle V_p \rangle$	$\langle V_s \rangle$	P	S	Azimuth	Pl	Strike	Dip
(km)	(g/cm ³)	(km/s)	(km/s)	anis.	anis.	(°)	(°)	(°)	(°)
1.76	2.622	5.550	2.640	0	0	N/A	N/A	0	0
19.00	2.612	6.193	3.643	6.2	0.2	5	18	0	0
26.00	2.651	6.102	3.998	9.9	0.2	323	3	0	0
half-space	3.221	8.220	4.580	0	0	N/A	N/A	170	3

Table 3. Range of inverted parameter values at CAN station related to anisotropy and a dipping Moho determined for the best 100 models.

Second layer	<i>P</i> anis.	5-7
	<i>S</i> anis.	0-2
	Azimuth (°)	0-13
	<i>Pl</i> (°)	0-7
Third layer	<i>P</i> anis.	9-10
	<i>S</i> anis.	0-1
	Azimuth (°)	309-352
	<i>Pl</i> (°)	16-24
Half-space	Strike (°)	170-176
	Dip (°)	2-4